Contents lists available at ScienceDirect

Geomorphology

Invited research article

Quantifying 40 years of rockfall activity in Yosemite Valley with historical Structure-from-Motion photogrammetry and terrestrial laser scanning

Antoine Guerin [a,*], Greg M. Stock [b], Mariah J. Radue [b], Michel Jaboyedoff [a], Brian D. Collins [c], Battista Matasci [a], Nikita Avdievitch [b], Marc-Henri Derron [a]

[a] Risk Analysis Group, Institute of Earth Sciences, University of Lausanne, Lausanne 1015, Switzerland
[b] U.S. National Park Service, Yosemite National Park, El Portal, CA 95318, USA
[c] U.S. Geological Survey, Landslide Hazards Program, Moffett Field, CA 94035, US

ARTICLE INFO

ABSTRACT

Rockfalls and rockslides are often dominant geomorphic processes in steep bedrock landscapes, but documenting their occurrence can be challenging, requiring frequent monitoring and well resolved spatial data. Repeat application of remote sensing methods such as Terrestrial Laser Scanning (TLS) and Structure-from-Motion (SfM) photogrammetry can detect even very small rockfalls, but typically these acquisitions span only years and may not record rockfall activity representative of longer-term rates of cliff erosion. Inventory databases can extend rockfall records, but are commonly incomplete and prone to observation bias. We employed TLS and SfM on two adjacent cliffs (El Capitan and Middle Brother) in Yosemite Valley, integrating semi-annual data collections from 2010 to 2017 with "historical" (archival) SfM models derived from oblique photographs taken in 1976. Comparing the 1976 SfM models against more recent data allows for more accurate and precise rockfall detection and volume measurement over a 40-year period. Change detection indicates that 235 rockfalls occurred from the two cliffs, more than twice as many events as are recorded in Yosemite's inventory database. Although individual rockfall volumes reported in the inventory database vary from those measured by SfM-TLS, reported cumulative volumes are similar to measured volumes, likely because the large-volume events that account for most of the cumulative volume tend to be widely observed and well-documented. Volume-frequency relationships indicate that the cliffs erode predominantly by less frequent, larger-volume rockfalls, at rates of 0.9 to 1.7 mm/yr. Our study demonstrates how integrated SfM and TLS measurements, especially utilizing SfM models derived from historical imagery, allow detection and quantification of rockfalls spanning several decades, complementing and improving inventory databases, informing rockfall hazard assessment, and providing longer-term rates of cliff erosion.

© 2020 Elsevier B.V. All rights reserved.

1. Introduction

Rockfalls from bedrock slopes are a primary means by which mountainous landscapes evolve (e.g., Wieczorek and Jäger, 1996; Matsuoka and Sakai, 1999; Krautblatter and Dikau, 2007; Moore et al., 2009). Geomorphic studies addressing rates of mountain landscape evolution therefore require accurate accounting of rockfalls and their volumes over known time intervals. However, because rockfalls often occur in remote settings, even large-volume events may escape detection. Furthermore, rates of cliff erosion are rarely steady when assessed over short timescales, with many cliffs characterized by sporadic pulses of rockfall activity interspersed with long periods of inactivity (e.g., Stock et al., 2018). The ability to accurately measure cliff erosion rates in rockfall-prone

settings therefore depends on accurate inventories of rockfall activity collected over sufficiently long time intervals, which may vary by geologic setting (Williams et al., 2019).

Remote sensing techniques such as Terrestrial Laser Scanning (TLS) and Structure-from-motion (SfM) photogrammetry have vastly improved rockfall detection, enabling a more accurate inventory of rockfalls (e.g., Rosser et al., 2005; Abellán et al., 2010; Williams et al., 2018, 2019; Gilham et al., 2019) and precise measurement of rockfall volumes (Stock et al., 2011; Carrea et al., 2015; Guerin et al., 2017), as well as pre- and post-event structural measurements (Pedrazzini et al., 2010; Heckmann et al., 2012; Roberti et al., 2018) and assessment of rockfall susceptibility (Dunham et al., 2017; Matasci et al., 2018; Zhang et al., 2019). The high fidelity of these methods usually allows for rockfall detection across a wide range of volumes, providing a near-complete inventory of rockfalls. However, because TLS and SfM methods have been applied to rockfall studies relatively recently, most applications span only relatively

short periods of time (on the order of years), and therefore may record sporadic periods of rockfall activity (or inactivity) that are not representative of longer-term rates.

Longer-term records of rockfall activity are sometimes provided by historical inventories, either for a specific cliff or for a larger region (e.g., Gardner, 1970; Luckman, 1976; Hungr et al., 1999; Dussauge et al., 2003; Chau et al., 2003; Stock et al., 2013). In addition to recording information about rockfall occurrence, such inventories can also offer valuable data for understanding environmental triggers (e.g., Sass and Oberlechner, 2012; Delonca et al., 2014; Letortu et al., 2015; Pratt et al., 2018), volume-frequency relationships (e.g., Guzzetti et al., 2003; Brunetti et al., 2009; Valagussa et al., 2014; De Biagi et al., 2017), and resulting hazard and risk (e.g., Corominas and Moya, 2008; Budetta and Nappi, 2013; Lari et al., 2014; Pellicani et al., 2016). These inventories have been collected primarily by park rangers, forest guards, geologists, and highway and railway workers along transportation corridors (Wieczorek et al., 1992; Hantz et al., 2003; Copons and Vilaplana, 2008; Lato et al., 2009; Kromer et al., 2015; van Veen et al., 2017; Voumard et al., 2018). As human observations are the primary source of documentation, rockfall inventory databases are subject to biases and inaccuracies that affect both the observation rate and the estimation of rockfall volumes (Luckman, 1976; Douglas, 1980; Dussauge-Peisser et al., 2002; Chau et al., 2003; Brunetti et al., 2009; Guzzetti et al., 2009; Rossi et al., 2010). These studies highlight a non-uniform observation rate over time, an under-representation of small events, and only rough volume estimates that are commonly based on the amount of material deposited (usually on a road, railway, or trail) rather than on volume changes on the slope. Based on geomorphological evidence, Brunetti et al. (2009) and Guzzetti et al. (2009) argue that the uncertainty associated with estimated rockfall volumes is usually within the same order of magnitude as the estimate itself.

An emerging method with potential to extend rockfall detection backwards in time involves SfM methods applied to "historical" (sometimes referred to as "archival") images (i.e., images taken prior to the advent of TLS or SfM methods). If the historical photographs have sufficient overlap and proper lighting conditions, it is possible to generate high-resolution terrain models of landscapes as they appeared at the time the photographs were taken. By "winding back the clock" on terrain model generation, historical SfM methods "*provide unexpected opportunities for the four-dimensional research of geomorphological processes*" (Eltner et al., 2016, p. 376, section 5.3). SfM utilizing archival orthophotos or oblique imagery has been used successfully to quantify surface elevation changes for volcanoes (Gomez, 2014; Derrien et al., 2015; Ishiguro et al., 2016), glaciers (Tonkin et al., 2016; Mertes et al., 2017; Midgley and Tonkin, 2017; Mölg and Bolch, 2017; Girod et al., 2018), coastal cliffs (Warrick et al., 2016; Esposito et al., 2018), river-floodplain systems (Gomez et al., 2015; Vautier et al., 2016; Bakker and Lane, 2017) and landforms subject to anthropogenic activities (Riquelme et al., 2019). A benefit of oblique photographs lies in the ability to generate SfM point clouds for very steep (vertical to over-hanging) terrain not suitably imaged in plan-view orthophotos. Using images taken prior to any dedicated remote sensing data acquisition effort, SfM can be used to reconstruct steep rock slopes prior to failure (Guerin et al., 2017; Voumard et al., 2017); these reconstructions then allow for more accurate calculation of past rockfall volumes by comparing against more recent SfM or TLS data. For instance, applying SfM methods to historical imagery refined the volume of a large rockfall that affected the west face of the Drus (Mont-Blanc massif, France) in June 2005 (Guerin et al., 2017); previously estimated from a single TLS point cloud acquired after the event (Ravanel and Deline, 2008), the rockfall volume increased from $265,000 \pm 10,000$ m^3 to $292,680 \pm 16,400$ m^3 using the new SfM dataset. Based on surface change measurements, the confidence level associated with both TLS and SfM-based volume measurements is much higher than those estimated in historical inventories, clearly illustrating the value of these methods.

Here we demonstrate the potential to couple SfM techniques utilizing historical photographs with more recent TLS data to greatly improve rockfall detection and measurement of rockfall volumes. These improvements allow us to assess rockfall volume-frequency relationships, measure cliff retreat rates, and evaluate the accuracy and completeness of a rockfall inventory database. We report the results of 40 years of rockfall activity from two cliffs in Yosemite Valley, the southeast faces of El Capitan and Middle Brother.

2. Study site

Yosemite Valley is a 1 km-deep, 14 km-long valley in the central Sierra Nevada mountain range of California (Fig. 1A). The bedrock is composed of massive Cretaceous granitic rocks of the Sierra Nevada batholith (Calkins et al., 1985; Bateman, 1992). River incision initially generated much of the relief of Yosemite Valley, but Pleistocene glacial erosion is responsible for the valley's width and vertiginous wall (Matthes, 1930; Huber, 1987). The last glacial period, known locally as the Tioga Glaciation, reached its maximum extent in the Sierra Nevada between 28 and 17 ka (Rood et al., 2011; Wahrhaftig et al., 2019). Deglaciation began about 19 ka, and Yosemite Valley is presumed to have been ice-free by about 15 ka (Stock and Uhrhammer, 2010). Following deglaciation, rockfalls from the glacially-steepened cliffs became the dominant erosional process, with large talus deposits accumulating beneath the cliffs (Wieczorek and Jäger, 1996). Although the broad topography of Yosemite Valley has developed along a network of regional fractures (Matthes, 1930; Huber, 1987; Matasci et al., 2011), the most common cliff fractures are sheeting, or exfoliation, joints formed parallel or subparallel to the modern topography (Matthes, 1930; Huber, 1987; Bahat et al., 1999; Martel, 2006, 2011). Sheeting joints form the primary detachment surfaces for most rockfalls in Yosemite (Wieczorek and Snyder, 1999; Stock et al., 2011, 2012).

Historical rockfalls in Yosemite National Park are documented in an inventory database that spans 160 years (1857–2018). Wieczorek et al. (1992) first compiled this information, with subsequent updates by Wieczorek and Snyder (2004) and Stock et al. (2013). By the end of 2018 the inventory database contained 1330 events, with estimated volumes spanning six orders of magnitude (approximately 0.02 to 200,000 m^3). From the first version of the database, Wieczorek et al. (1992) recognized that the recording of smaller and less consequential rockfalls has not always been systematic, and that the inventory was incomplete for volumes less than about 100 m^3 (Wieczorek et al., 1995). The inventory has three types of categories (Stock et al., 2013) assigned to rockfall volumes: (1) the reported volume is well-constrained and precisely measured from Terrestrial Laser Scanning (TLS) and/or Structure-from-Motion (SfM) photogrammetry data (Stock et al., 2011, 2012, 2018; Zimmer et al., 2012); (2) the volume was not precisely measured but can be constrained by a wide range of field observations (accuracy better than an order of magnitude) (e.g., Snyder, 1986, 1996; Wieczorek and Snyder, 1999; Wieczorek et al., 1995, 2000, 2008); (3) no or only vague indication of size is specified (this is the case for most events prior to 1980) and the reported volume is assigned an order-of-magnitude estimate with values equal to 20 m^3, 200 m^3, 2000 m^3, etc. (e.g., Wieczorek et al., 1992; Wieczorek and Jäger, 1996; Wieczorek, 2002). Prior to the advent of TLS and SfM techniques, volumes of rockfalls from the steep, inaccessible cliffs of Yosemite Valley were primarily obtained by estimating the length and width of the rockfall scar based on nearby features with approximately known sizes, such as trees or climbing pitches, and with little to no accounting for complex scar geometries. The thickness of the failed rock mass within the rockfall scar was usually estimated with few constraints. Thus, a number of factors contribute to volumetric errors in the database.

This study investigates rockfalls from two adjacent cliffs on the north side of Yosemite Valley: the southeast face of Middle Brother and the southeast face of El Capitan (Fig. 1). Both cliffs are within the spatial limit of the Tioga Glaciation, but El Capitan experienced less glacial
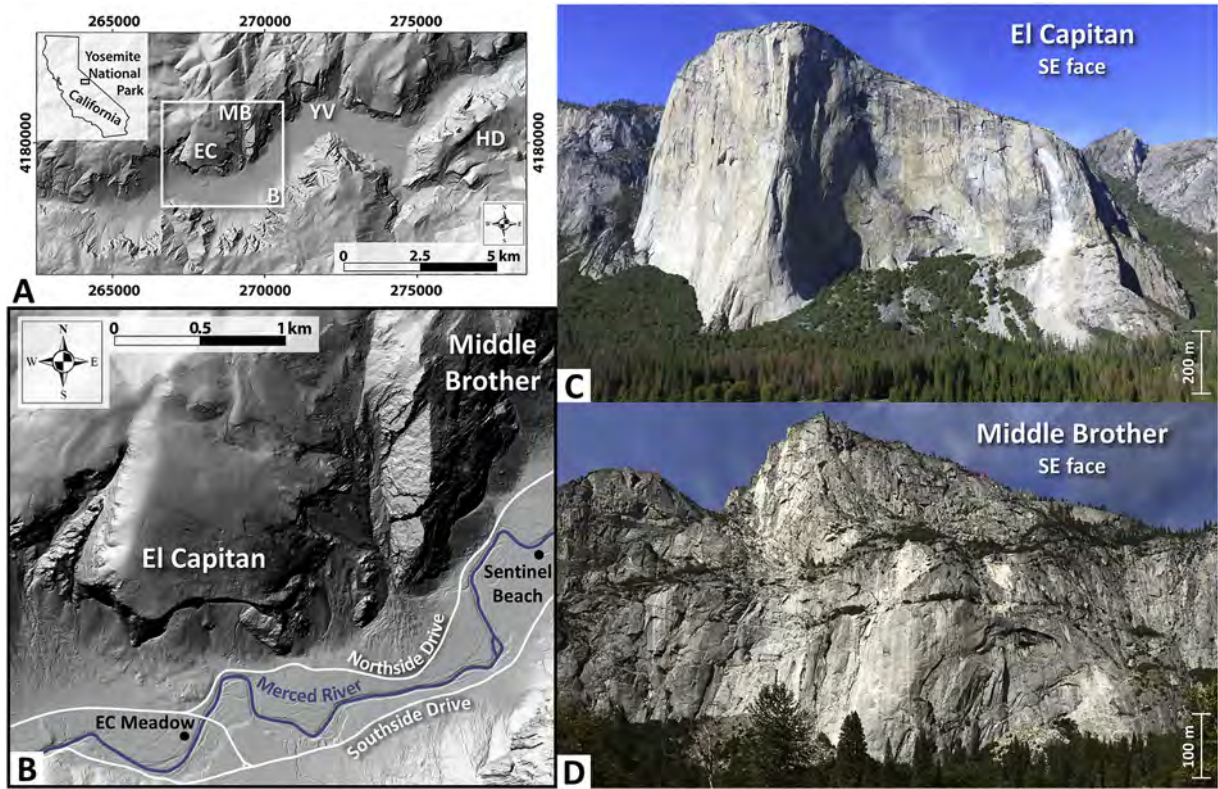
Fig. 1. Locations of the two monitored cliffs in Yosemite Valley. **(A)** Aerial laser scanning DEM (1 m × 1 m cell size resolution) of Yosemite Valley. Key to abbreviations: EC = El Capitan; HD = Half Dome; MB = Middle Brother; YV = Yosemite Village. **(B)** Detail of El Capitan and Middle Brother areas framed in Panel A. Black dots indicate the locations of TLS acquisitions. **(C)** SE face of El Capitan in Oct. 2017 (a few days after the rockfall events on 27–28 Sep. 2017). **(D)** SE face of Middle Brother in Oct. 2016 taken from Sentinel Beach.

erosion being closer to the glacier terminus and therefore having a smaller area of ice cover (Wahrhaftig et al., 2019). Both cliffs are composed of granitic bedrock. The southeast face of El Capitan is composed predominantly of El Capitan Granite, with about 30% Taft Granite and 20% intrusive quartz diorite (Calkins et al., 1985; Peck, 2002; Putnam et al., 2015). The southeast face of Middle Brother is composed predominantly of Sentinel Granodiorite with approximately 30% Half Dome Granodiorite and 5% El Capitan Granite (Calkins et al., 1985; Peck, 2002).

3. Materials and methods

3.1. TLS specifications and baseline data collection

We utilized multiple TLS and SfM data sources for our analyses, spanning 41 years (Fig. 2). TLS point clouds represent the baseline remote sensing data in our monitoring. TLS data served as references for all change detection analyses, and georeferenced TLS data also allowed us to rescale and align the SfM models.

We collected five TLS point cloud datasets for both Middle Brother and El Capitan between 2010 and 2016. The first dataset was collected in October 2010 using an Optech ILRIS-3D-ER scanner, while the following four datasets were collected in June 2012, October 2013, October 2015, and October 2016 using an Optech ILRIS-LR scanner. These two scanners are characterized by a manufacturer-specified accuracy of 7 mm at a range of 100 m and a maximum point-to-point density of 2 cm at a range of 1000 m (Teledyne Optech, 2019).

TLS data were acquired from El Capitan Meadow and Sentinel Beach (Fig. 1B), located approximately 1100 m and 950 m from El Capitan and Middle Brother respectively. For each of these cliffs, the resulting TLS models consist of 38.1 and 35.7 million points, with a mean point-to-point spacing of 15 cm (i.e. ~40 pts./m²) (we refer to a mean spacing because the TLS-cliff distance increases between the bottom and the top of
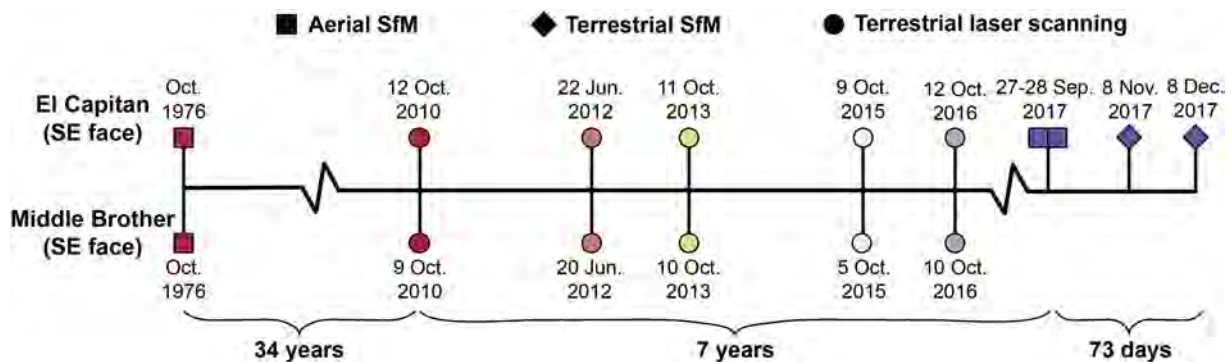

Fig. 2. Timeline of Structure-from-Motion photogrammetry (SfM) and terrestrial laser scanning (TLS) acquisitions for the southeast faces of El Capitan and Middle Brother. Note that the timescale is not linear, with monitoring intervals ranging from days to years. Colors correspond to the colorbars of Figs. 6 and 8.

the cliffs). Because of increasing upward TLS scanner to cliff distance, a decreasing resolution gradient up the rock face limits the detection of smaller rockfalls in the upper part of both cliffs. We aligned and scaled the 2010 point clouds onto an existing 1 m aerial Digital ElevationF Model (DEM) of Yosemite Valley using Iterative Closest Point (ICP) algorithms (Besl and McKay, 1992; Chen and Medioni, 1992) implemented in CloudCompare software (version 2.7.0; Girardeau-Montaut, 2015). The Root Mean Square Error (RMSE) values associated with the georeferencing process are 0.44 m and 0.31 m, for El Capitan and Middle Brother respectively. The 2010 point clouds were then converted to triangular reference meshes using Poisson surface reconstruction algorithms (Kazhdan et al., 2006) implemented in 3DReshaper software (version 10.1.4; Hexagon-Technodigit, 2015). Cliff surface areas measured on the meshes are 537,820 m^2 for the southeast face of El Capitan and 1,063,600 m^2 for the southeast face of Middle Brother. All successive TLS point clouds were aligned to the 2010 meshes by applying point-to-surface ICP algorithms (Zhang, 1994). As recommended by many studies (e.g., Teza et al., 2007; Oppikofer et al., 2009; Royán et al., 2014; Kromer et al., 2015; Rowe et al., 2018), these algorithms

were only applied to manually selected "stable areas" by way of photographic visual inspections (areas for which no change has been identified between two dates) to optimize the registration accuracy. Thus, the areas having undergone significant changes between 2010 and 2016 were aligned according to the roto-translation matrices obtained in stable areas. Before noise filtering (Section 3.4), an average point-to-surface standard deviation of ± 3.6 cm (confidence interval given by 2σ) characterizes the alignment of TLS scans in stable areas.

3.2. Historical oblique photographs

To reconstruct the former topography of the southeast faces of El Capitan and Middle Brother, we used 16 and 21 oblique photographs, respectively. A member of Yosemite's Search & Rescue team took these photographs from a helicopter in October 1976 for the purpose of planning and executing cliff rescues. The photographs were taken for visual reference only (i.e., not originally intended for photogrammetry). The photographs were taken with a single lens reflex camera
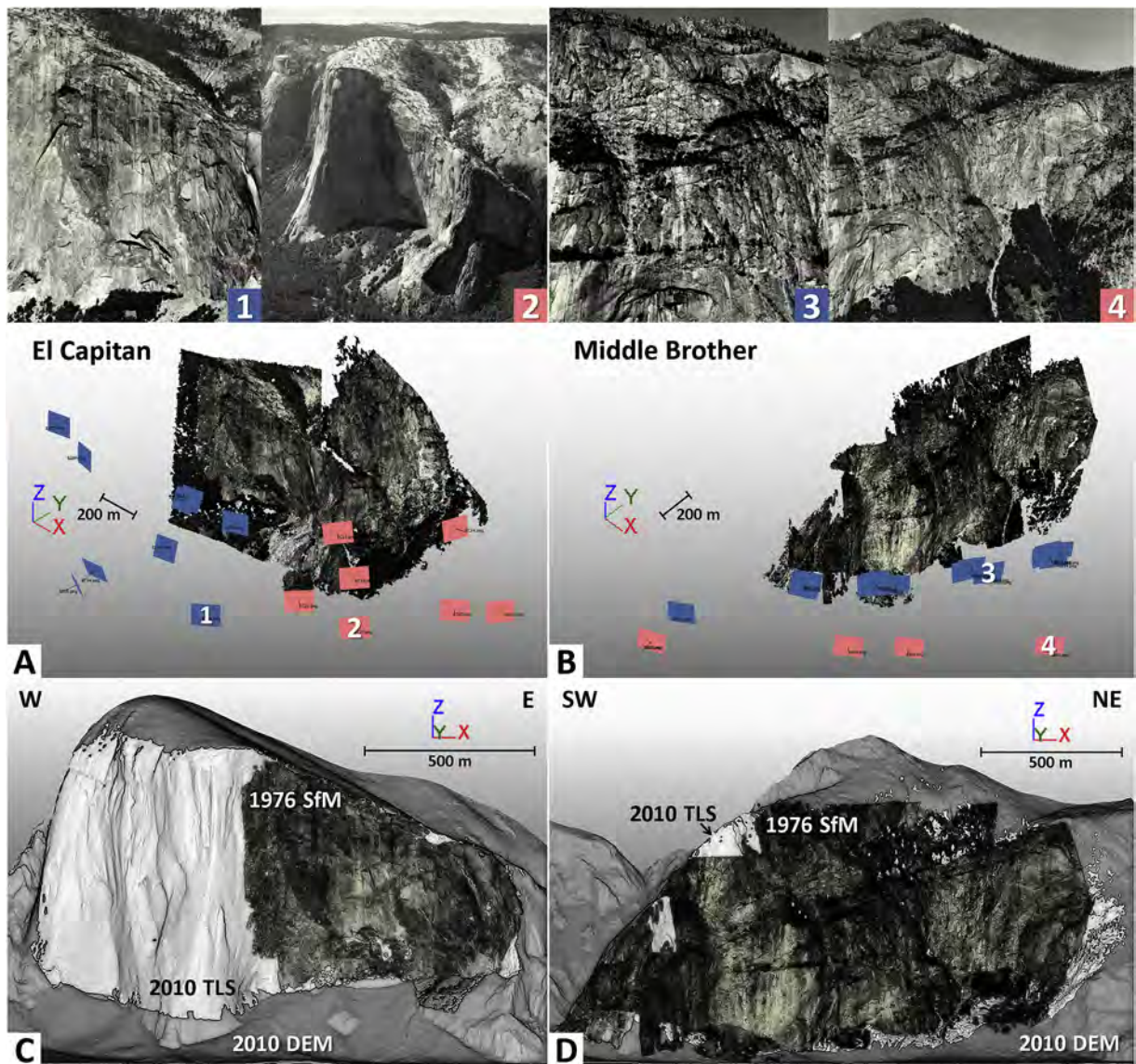

Fig. 3. Black and white photographs and historical SfM models of El Capitan and Middle Brother. **(A)** and **(B)** Examples of oblique helicopter photographs used for topographic reconstruction of the SE faces of El Capitan and Middle Brother(upper panels) and oblique presentation of the corresponding 1976 SfM models (lower panels) that include camera positions and orientations (rectangle symbols). Blue color indicates close-up shots; pink color indicates distant shots. **(C)** and **(D)** Superimposition of the 2010 aerial laser scanning DEM with the 2010 TLS reference mesh and the 1976 SfM point cloud after all registration and scaling processes. (For interpretation of the references to color in this figure legend, the reader is referred to the web version of this article.)

on black-and-white film, and were acquired from different distances, such that the series includes close-up views and overviews of both cliffs (Fig. 3; Supplementary Figs. 1 and 2), with an overlap ranging from 20 to 70%. The photographs were taken at mid-day with low sun angles under a bright and slightly cloudy sky, minimizing shadows in overhanging sections of these southeast-facing cliffs (Fig. 3; Supplementary Figs. 1 and 2), although in the case of El Capitan, two overview photos acquired later in the afternoon show the southeast face half-shaded (Fig. 3; Supplementary Fig. 1). The 37 photographs were digitized into JPEG-format at a resolution of 300 dpi (2950 × 2400 pixels), with an average size of 650 KB, on a standard film scanner.

We also collected additional SfM model data following a rockfall sequence that affected El Capitan between September and November 2017; for this rockfall, four SfM models were created for the easternmost part of the southeast face (Stock et al., 2018). The first two photographic surveys (27 and 28 September 2017) consisted of approximately 200 photographs each, acquired from a helicopter with a Panasonic Lumix DMC-TS3 camera set to a wide-angle (5 mm focal length) to address the short distances to the cliff. The other two surveys were conducted from the ground on 6 November and 7 December 2017, with a Canon EOS 50D camera and a focal length fixed at 300 mm. Photos were geotagged to aid in initial registration. The average size of these recent photographs is 50 MB and the resolution of both cameras is 4000 × 3000 pixels and 4752 × 3168 pixels respectively. The amount of overlap between photographs ranges between 60 and 80%.

3.3. Georeferenced SfM model generation

We constructed SfM point cloud models using the commercially available Agisoft PhotoScan Professional Edition software (version 1.0.4; Agisoft, 2014). Image processing follows the SfM workflow and involves: (1) the application of a mask over unwanted parts of the photographs (e.g., white borders, numbering, helicopter blades), (2) an automatic image alignment that generates a sparse model with the extracted keypoints (<0.1 million points in our case), and (3) the building of a very dense point cloud (>5 million points in our case) after calculating depth maps for every picture (e.g., Smith et al., 2016). Unlike many studies (e.g., Westoby et al., 2012; Lucieer et al., 2014; Manousakis et al., 2016; Girod et al., 2018; Kumar et al., 2018; Török et al., 2018), no ground control points were used to set up the coordinates system when generating SfM models. As we already had georeferenced TLS data, we scaled and georeferenced the SfM data using the method defined by Guerin et al. (2017). This method consists of four steps: (1) a rough scaling based on dimensions measured on the 2010 TLS meshes, (2) a global point-to-surface ICP alignment, (3) a segmentation of the meshes/point clouds into hundreds of cubes using the octree structure (e.g., Woo et al., 2002), and (4) independent scaling and alignment of each SfM subset to the corresponding TLS subset using point-to-surface ICP algorithms. It should be noted that step 4 makes it possible to significantly reduce the "doming deformation" (Rosnell and Honkavaara, 2012; James and Robson, 2014; Javernick et al., 2014; Ruggles et al., 2016) specific to SfM models, by allowing subsets of the SfM model to transform independently of each other; it is this processing step that eliminates the need for ground control points.

The resulting 1976 SfM models (Fig. 3C and D) consist respectively of 5.3 and 5.9 million points, with a point-to-point spacing of 27 cm for El Capitan and 45 cm for Middle Brother (i.e. ~14 pts/m² and ~5 pts/m²). Due to insufficient overlap of four photos, the top and westernmost portions of Middle Brother could not be reconstructed (Fig. 3D). Given the smaller cliff area of interest, the larger number and higher resolution of photographs, and SfM-dedicated photo collection techniques, the resulting 2017 SfM models have a higher spatial resolution, with a point-to-point spacing of 9 cm and 5 cm in the area of interest, for

helicopter- and ground-based surveys respectively. Before noise filtering, the point-to-surface standard deviations (confidence interval given by ±2σ) of SfM point clouds in stable areas are distributed as follows: ±28 cm for the 1976 El Capitan model, ±42 cm for the 1976 Middle Brother model, ±8.1 cm for the September 2017 El Capitan models, and ± 4.7 cm for the November–December 2017 El Capitan models.

3.4. Change detection and noise filtering

Change detection between all 3-D models was carried out by performing point-to-mesh comparisons in chronological order. We calculated distances between two successive acquisitions (e.g., 2012 and 2013 TLS data sets) by choosing the oldest data as reference for the generation of the mesh, with the exception of the 1976 point clouds, where the reference data was set to 2010 (Figs. 4A and 7). At the end of the calculation, a scalar value corresponding to the shortest orthogonal distance between a point and the nearest triangle of the mesh (Kiryati and Székely, 1993) is associated with each point. Positive and negative surface changes are respectively due to a gain (e.g., debris accumulation, vegetation changes) or a loss (e.g., rockfalls, impacts) of material.

To reduce the influence of instrumental TLS noise, the residual doming deformation and local spikes in elevation (Guerin et al., 2017) of the SfM models, we applied a spatial noise filter to the raw point-to-mesh differences (Abellán et al., 2009). This filtering algorithm allows denoising the raw distances using nearest neighbor averaging; for this study, we used 50 neighbors for the averaging process. This value is representative of a planar cliff surface of 4.5 m² for El Capitan and 10 m² for Middle Brother. Based on Gaussian statistics described by Lague et al. (2013), we selected the confidence intervals given by ±2σ to define the levels of detection at 95% (LoD95%) of each comparison. The point-to-surface standard deviations of the smoothed comparisons are distributed as follows: ±18 cm for the 1976 El Capitan model (SfM vs. TLS), ±34 cm for the 1976 Middle Brother model (SfM vs. TLS), ± 2.2 cm for TLS data (TLS vs. TLS), ±6.9 cm for the September 2017 El Capitan models (SfM vs. TLS) and ±3.8 cm for the November–December 2017 El Capitan models (SfM vs. SfM).

3.5. Analysis of surface changes detected using historical SfM models

3.5.1. Interpretation of positive deviations

After a thorough visual inspection of photographs, all positive deviations detected between the 1976 and 2010 (SfM vs. TLS) datasets could be assigned either to border effects (due to lens distortion) or vegetation changes (Figs. 4A and 7). As a result, we did not detect any major outward displacement greater than +2σ (+18 cm for El Capitan and +34 cm for Middle Brother) associated with rock deformation. The same observation is true for the 2016–2017 comparisons combining SfM and TLS data (Fig. 5A). However, an outward rotational movement up to 20 cm involving a rock sheet 23 m tall by 14 m wide was detected between 28 September and 6 November 2017 (Stock et al., 2018) and confirmed by field observation. This sheet of several tens of cm thick was likely displaced during or immediately after a rockfall on 22 October 2017, which originated from just below the displaced sheet (Stock et al., 2018).

3.5.2. Interpretation of negative deviations

Visual inspections were also helpful in classifying the detected negative surface changes and isolating artifacts generated by an inaccurate reconstruction of the topography in the 1976 SfM models. This analysis resulted in the identification of two types of artifacts, located in: (1) concave and overhanging areas that generate shadows at mid-day (Figs. 4A, 7 (horizontal ellipses), 10 and 11), and (2) areas where the overlap between two photographs was insufficient (<20%). This second artifact was only observed twice in the lower part of Middle Brother (Fig. 7; vertical ellipses) and is characterized by a shift of about +3 m (the SfM points appear in front of the TLS

points) that extends vertically over several hundred meters. Except for the examples framed in Fig. 4A (true rockfalls), the anomalies generated by the first type of artifact are far more numerous and scattered across the cliff (Figs. 7, 10 and 11). Therefore, we performed a systematic photographic comparison between 1976 and 2010 (Figs. 10 and 11) to manually separate the true rockfalls from false records detected. Regarding

the 2017 SfM models, only the first type of artifact remains in the form of sparse measurement noise with an average amplitude of −10 cm (Fig. 5A). This negative anomaly was removed automatically during the noise filtering process.

Following the visual inspections, only four rockfalls (volumes between 93 m³ and 2019 m³) that occurred between October 1976 and
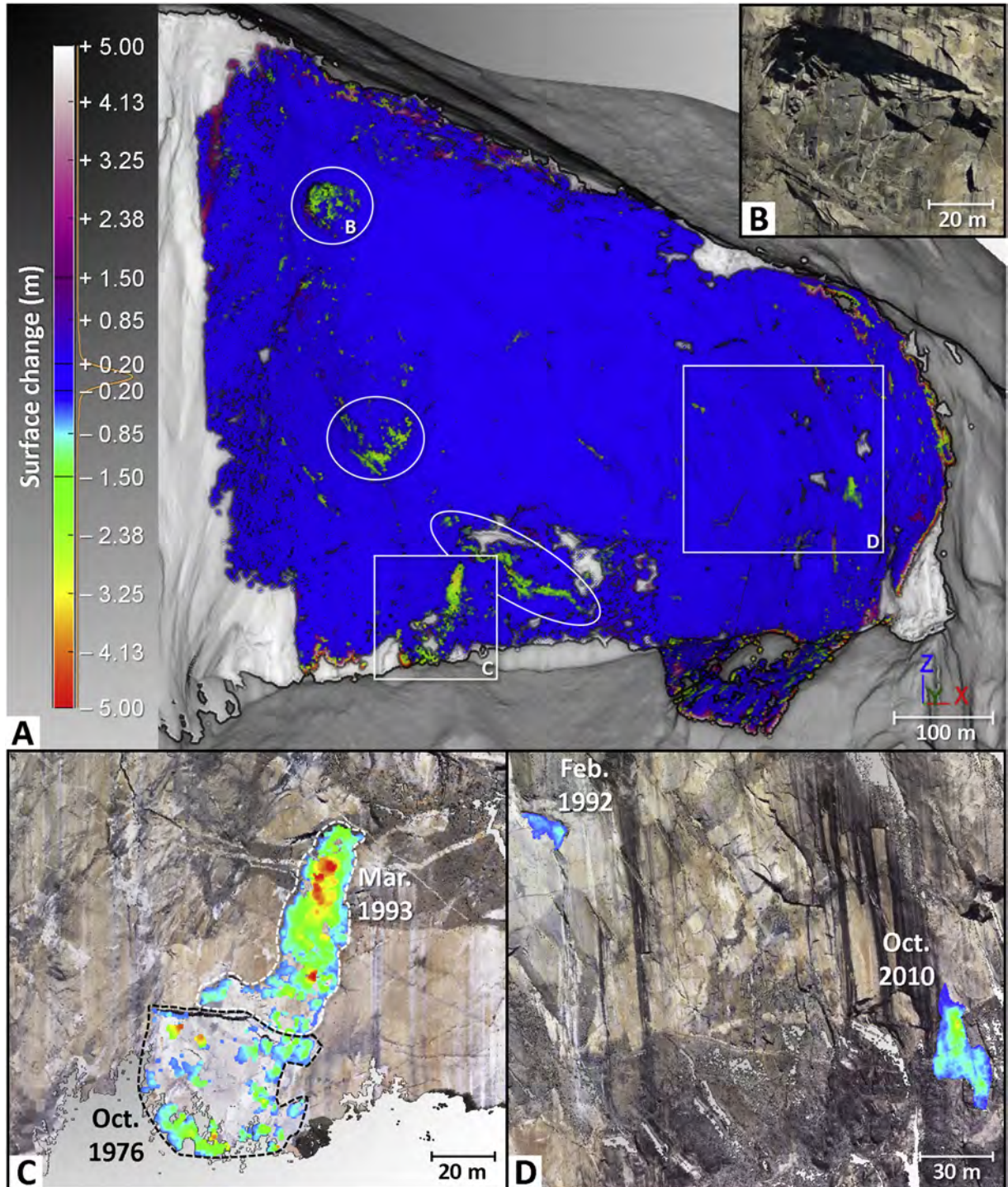

Fig. 4. Results of the comparison between Oct. 1976 and Oct. 2010 data for the SE face of El Capitan. (**A**) Filtered point-to-mesh differences between the 1976 SfM point cloud and the 2010 TLS mesh. Positive deviations are associated with border effects and vegetation. Blue areas have differences less than the change detection uncertainty of ±0.18 m. Negative surface changes correspond either artifacts related to the presence of concave and overhanging areas (ellipses) or to rockfalls (squares). (**B**) Detail of the uppermost concave area circled in Panel A. (**C**) and (**D**) Detail of the surface changes associated with 4 rockfalls detected between 1976 and 2010. Colors are the same as those of Panel A and represents rockfall thicknesses; volumes are specified in Fig. 6 and Table 1. Background topographic surface: 2010 TLS mesh textured with gigapixel images. (For interpretation of the references to color in this figure legend, the reader is referred to the web version of this article.)
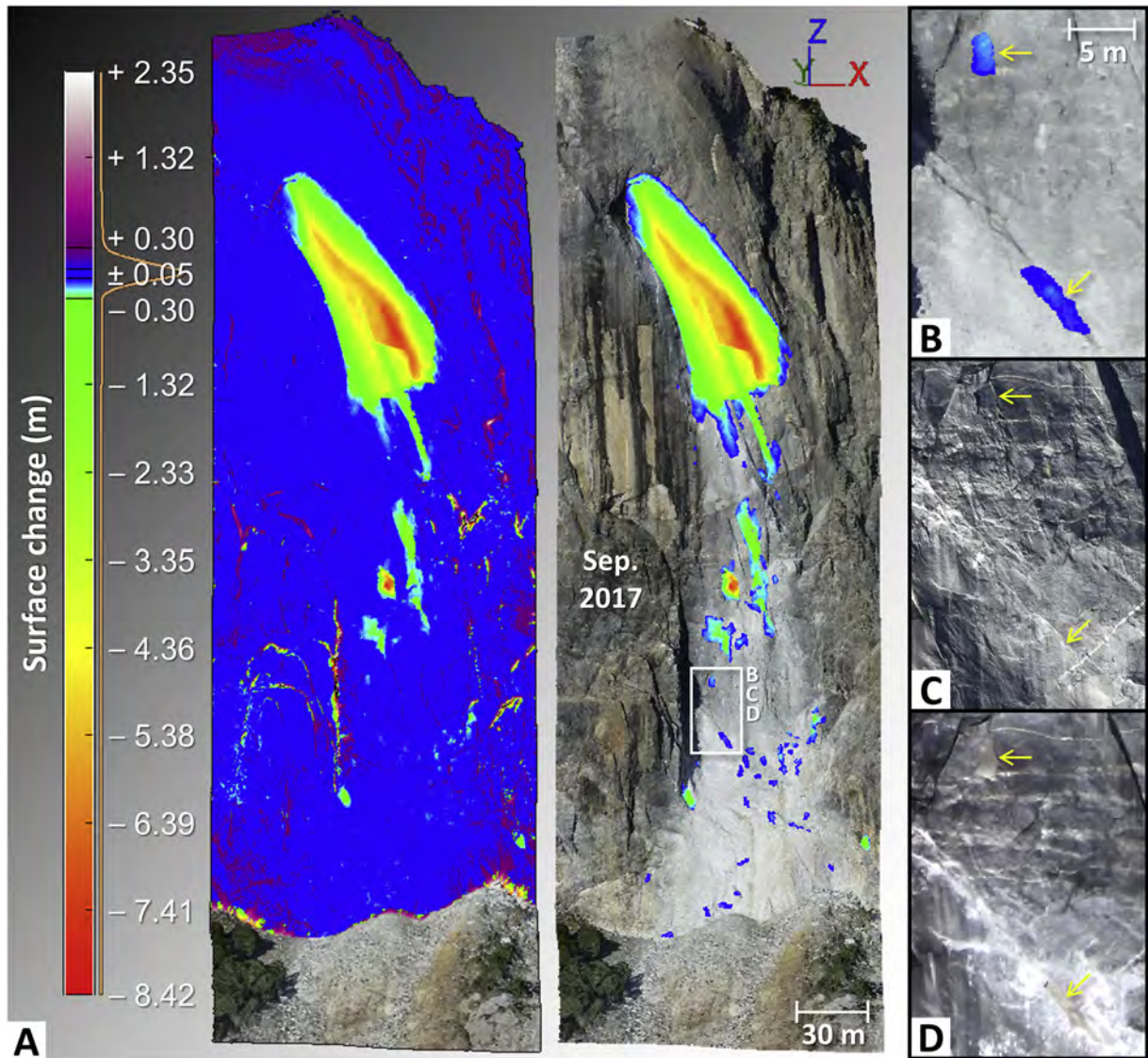
Fig. 5. Results of the comparison between Oct. 2016 and Sep. 2017 data for the easternmost part of El Capitan. **(A)** Filtered point-to-mesh differences between the 2016 TLS mesh and the 2017 SfM point cloud. Positive deviations are associated with border effects. Blue areas have differences less than the change detection uncertainty of ±0.069 m. Negative surface changes correspond to detachment areas, i.e. 46 rockfalls ranging from 0.04 m³ to 9811 m³; this number includes rock detached by impact from rockfalls above. Background topographic surface: 28 Sep. 2017 SfM model. **(B)** Detail of the area framed in Panel A; each arrow indicates the location of a rockfall. **(C)** and **(D)** Before-after comparison of the area shown in Panel B, showing rockfall scars. (For interpretation of the references to color in this figure legend, the reader is referred to the web version of this article.)

October 2010 could be clearly identified from the southeast face of El Capitan (Figs. 4 and 6). Using the extensive information reported in the inventory database (Stock et al., 2013), these four rockfalls could be dated precisely since the year, month and sometimes day were recorded. In addition, valuable information gathered from witnesses of the 3 October 1976 rockfall (Dale Bard, pers. comm. and Chris Falkenstein, writ. comm.) made it possible to precisely delineate the maximum extent of this event (Fig. 4B), located at the base of the March 1993 rockfall event (Fig. 4B). The upper part of the volume detected in this area could thus be associated with this more recent rockfall (Fig. 4B). Without the inventory database, only one rockfall (and only one volume) would have been identified in this area, thus distorting the rockfall detection between 1976 and 2010. Still, it is likely that these four rockfalls have collapsed into several compartments and that the number of falls associated with the 1976–2010 period is actually higher. This detection limit, due to the effects of superimposition (overlapping of sequential rockfall scars through time) and coalescence (amalgamation of adjacent rockfall scars) of rockfalls (van Veen et al., 2017; Williams et al., 2018, 2019), probably also applies to the

results from TLS comparisons (monitoring interval of 1.5 year in average; Fig. 2).

During the 2017 El Capitan rockfall sequence, change detection between four SfM models identified 58 rockfalls (volumes between 0.04 m³ and 9811 m³) between 27 September and 30 November 2017 (Stock et al., 2018). By way comparison, 53 rockfalls (volumes between 0.02 m³ and 977 m³) were detected using TLS data between October 2010 and September 2017.

For Middle Brother, 10 rockfalls (volumes between 31 m³ and 20,193 m³) were identified between October 1976 and October 2010 (Figs. 7 and 8). During this time period, the four largest rockfalls (>4770 m³) occurred in winter (February and March) in the upper half of the southeast face (Fig. 7). Between October 2010 and October 2016, TLS surveys have identified 110 rockfalls with volumes ranging from 0.02 m³ to 2844 m³ (Fig. 8; Supplementary Fig. 3). The increase in the number of rockfalls detected during this time period compared to 1976–2010, as well as the decrease in the minimum volume detected, results from the increased resolution of the TLS models and the more frequent monitoring.
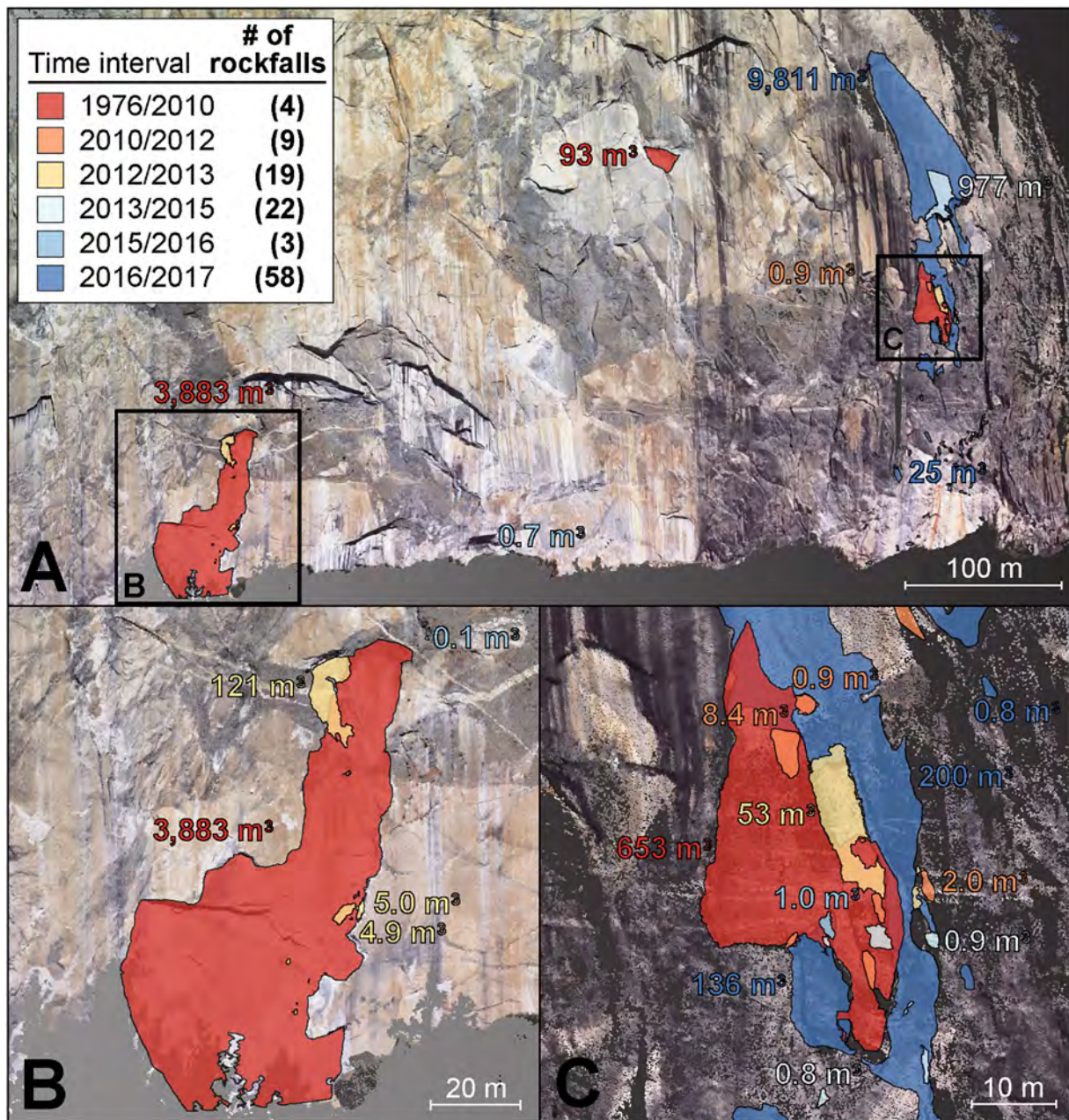
Fig. 6. 41 years of rockfall activity highlighted for El Capitan by means of SfM-TLS monitoring. **(A)** 115 rockfalls ranging from 0.02 m^3 to 9811 m^3 were detected between Oct. 1976 and Nov. 2017. Colors assigned to the different monitoring periods allow tracking the spatial and temporal progression of rockfalls. Background topographic surface: 2016 TLS mesh textured with a gigapixel panorama. **(B)** Detail of the 1976–1993 rockfall area framed in Panel A. Rockfalls from 1976 and 1993 (Fig. 4C) have been merged to give a volume of 3883 m^3. 15 rockfalls were detected in this scar since Oct. 2010. **(C)** Detail of the 11 Oct. 2010 rockfall scar area framed in Panel A. 25 rockfalls were detected within this scar since Oct. 2010.

3.6. Rockfall extraction and volume calculation

The rockfall identification process used here is described in Guerin et al. (2017). It is based on the method developed by Tonini and Abellán (2014) and involves (1) definition of a LoD$_{95\%}$ and assignment of three distinct colors to separate positive deviations, the deviations contained within the LoD$_{95\%}$, and negative deviations, (2) filtering of the three colors defined in the previous step, (3) filtering of residual noise using a distance criterion that is based on the spatial density of points in 3-D (nearest-neighbor clutter removal method of Byers and Raftery, 1998), and (4) extraction of individual rockfall areas using the DBSCAN algorithm (Ester et al., 1996).

We calculated all rockfall volumes according to the method outlined by Guerin et al. (2017). Each volume is defined by the sum of the tetrahedron volumes contained inside a closed mesh generated from the

reference mesh and the point cloud to which it is compared. However, it should be noted that the smoothing procedure was only applied to the 1976 SfM point clouds; it allows interpolation of new triangles to smooth the artifacts (spikes in elevation) present on the surface of rockfalls (pre-event topography). The uncertainty in our volume calculations depends the chosen LoD$_{95\%}$ (which includes the registration error and the residual noise) and the surface area of each rockfall. Given that the area is multiplied by the LoD$_{95\%}$, the geometric features of rockfalls strongly influences the volume uncertainty. For our error calculations, four geometric shapes were used to represent the rockfalls: square, rectangular, triangular, and complex (association of at least two of the three geometries above mentioned). Although the volume uncertainty depends on the resolution of the point clouds and decreases with larger volumes, it clearly appears (examples in Table 1) that the use of complex geometries (which are more faithful to the actual shape of
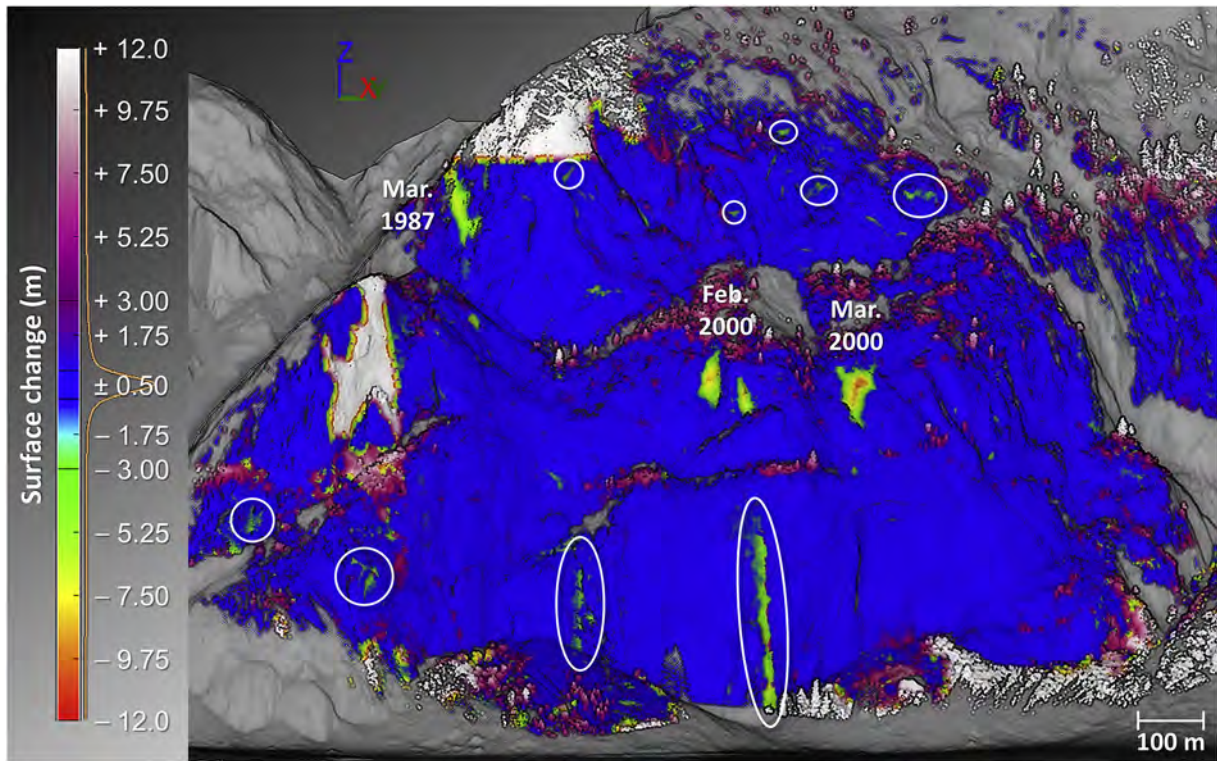
Fig. 7. Results of the comparison between Oct. 1976 and Oct. 2010 for the SE face of Middle Brother. **(A)** Filtered point-to-mesh differences between the 1976 SfM point cloud and the 2010 TLS mesh. Positive deviations are associated with border effects and vegetation. Blue areas have differences less than the change detection uncertainty of ±0.34 m. Negative surface changes correspond either artifacts related to the presence of overhangs (horizontal ellipses) and insufficient overlap between photographs (vertical ellipses) or to rockfalls. 10 rockfalls were detected during this period (the date of the largest ones is indicated); the volumes are specified in Fig. 8A. (For interpretation of the references to color in this figure legend, the reader is referred to the web version of this article.)

rockfalls) decreases the margin of error on the volume estimate. More specifically, our rockfall volume uncertainty varies between 13.0% and 39.8% (average value: 20.7%) for archival SfM (Table 1), between 2.9% and 28.7% (average value: 13.9%) for TLS (Stock et al., 2018), and between 4.2% and 36.0% (average value: 15.3%) for recent SfM (Stock et al., 2018).

3.7. Rockfall volume-frequency relationships

Landslides size distributions (related to surfaces or volumes) are generally known to follow negative power-laws (Stark and Hovius, 2001; Guzzetti et al., 2002; Malamud et al., 2004; Brunetti et al., 2009). The negative relationship implies that the frequency decreases as the volume increases. Fitting cumulative rockfall volume-frequency relationships to a power-law has been performed in many studies (e.g., Hungr et al., 1999; Picarelli et al., 2005; Barlow et al., 2012; Williams et al., 2018) with volume distributions of the form:

$$N(v>V) = aV^{-b} \tag{1}$$

where $N(v > V)$ is the number of rockfalls larger than the rockfall volume V, a is the intercept, and b is the exponent (Brunetti et al., 2009). The a parameter is directly linked to rockfall activity, as it represents the frequency of rockfalls, and the b exponent gives the slope of the power-law. More specifically, the b value reflects the spreading of the volume distribution; when the b value approaches 1, "*the volume of material contributed by larger events approaches unity with that contributed by smaller events*" (Barlow et al., 2012, p. 419, section 3.3). Thus, a b value <1 indicates that the volume distribution is skewed toward larger-volume events, whereas a b value >1 indicates that the volume distribution is skewed toward smaller-volume events. The power-laws derived from historical rockfall inventories tend to show that b appears to be

mainly influenced by the rock type and the structure of the rock mass (Gardner, 1970, 1983; Wieczorek et al., 1995; Hungr et al., 1999; Dussauge et al., 2003; Guzzetti et al., 2003; Hantz et al., 2003; Brunetti et al., 2009).

To determine the best fit and the best validity domain of the power laws adjusted to our data (Table 2), we used the maximum likelihood method (Pickering et al., 1995; Dussauge et al., 2003; Clauset et al., 2009; Williams et al., 2019). Assuming a pure power law distribution (Aki, 1965), the maximum likelihood estimate for b is:

$$b = \frac{1}{\ln(10) \left[< log(V)> - log(V_0)\right]} \tag{2}$$

with a standard deviation defined by:

$$\sigma = \frac{b}{\sqrt{N_0}} \tag{3}$$

where V_0 is the minimum volume used in the power law fit, $<log(V)>$ is the average of $log(V)$ for events larger than V_0, and N_0 is the number of events with volumes larger than V_0. In addition to the correlation coefficient R^2, we estimated two goodness-of-fit indicators (Table 2) to test whether the fitting of a power law distribution is plausible based on the values determined for b and V_0. These are the so-called Sum of Squared estimate of Errors (SSE) and Root Mean Squared Error (RMSE), which respectively measure the total deviation between the observed data values and the values predicted by the modeled distribution and the average deviation between the observed data and the modeled data. A value of R^2 close to 1 and values of SSE and RMSE close to zero reflect a good ability of the model to accurately predict the data.

In order to compare rockfall activities (given by the a-value) from cliffs of different sizes and surface areas (e.g., the southeast faces of El
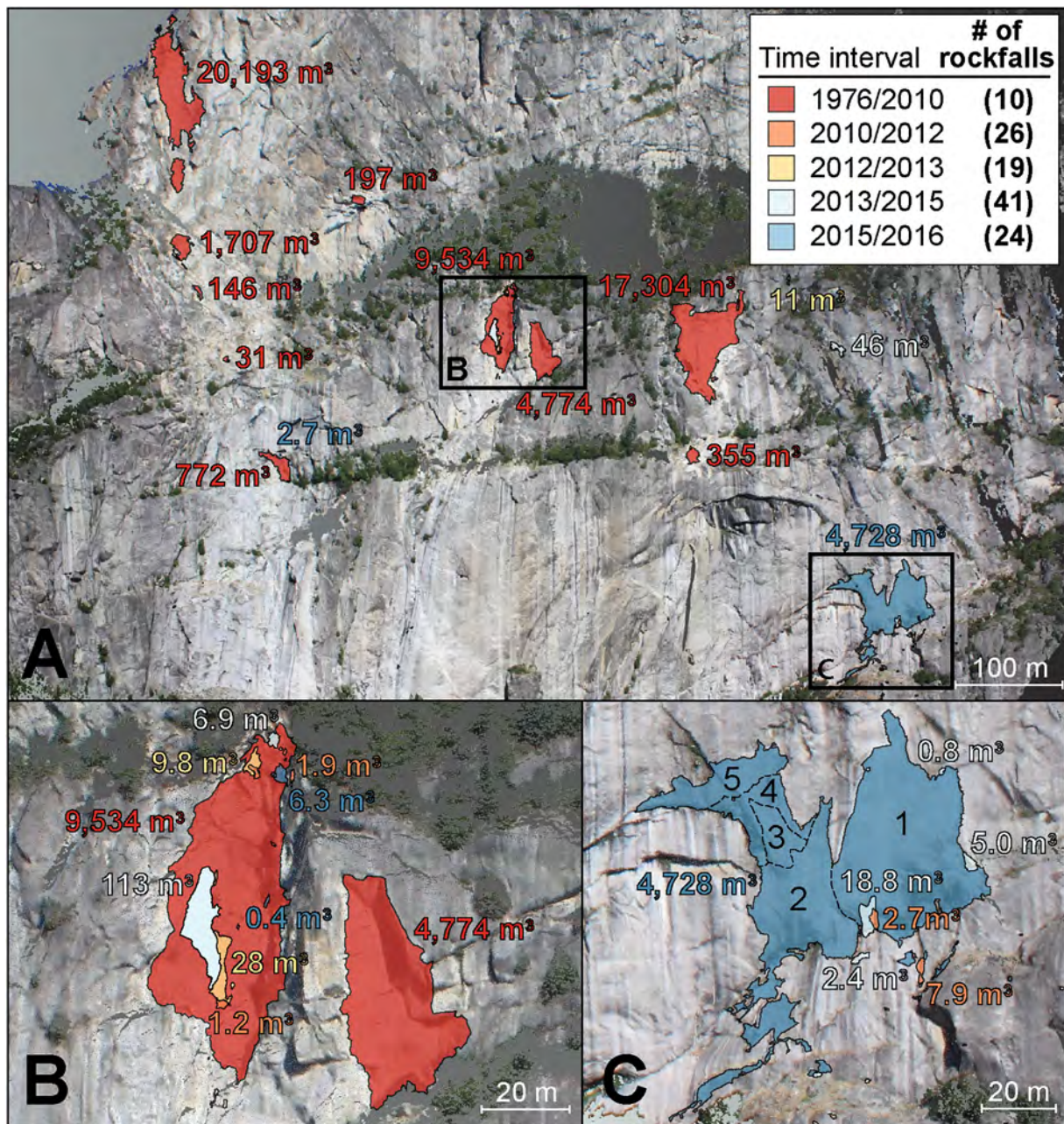
Fig. 8. 40 years of rockfall activity highlighted for Middle Brother by means of SfM-TLS monitoring. **(A)** 120 rockfalls ranging from 0.02 m³ to 20,193 m³ were detected between Oct. 1976 and Oct. 2016. Colors assigned to the different monitoring period allow tracking the spatial and temporal progression of rockfalls. Background topographic surface: 2016 TLS mesh textured with a gigapixel panorama. **(B)** Detail of the 22 Feb. 2000 rockfall scar areas framed in Panel A. 18 rockfalls were identified in the western (left) scar since Oct. 2010, whereas none were detected in the eastern scar over the same period. **(C)** Detail of the progressive 2015–2016 rockfall scar area framed in Panel A. Volume and timing of the numbered rockfalls: 1 = 2844 m³ (from 28 Oct. 2015 to 9 Mar. 2016); 2 = 991 m³ (31 Mar. 2016); 3 = 316 m³ (5 Aug. 2016, 08:11 PST); 4 = 248 m³ (5 Aug. 2016, 08:32 PST); 5 = 329 m³ (5 Aug. 2016, 12:30 PST).

Table 1
Quantitative volumetric comparison of the largest rockfalls that occurred in the SE faces of El Capitan (EC) and Middle Brother (MB) between 1976 and 2010. Geometric shape used to represent the rockfalls (volume uncertainty calculations): C = complex; S = square; R = rectangle; T = triangle. Except for the 10 Mar. 1987 volume noted in italics, the volumes from the Yosemite rockfall inventory database that do not explicitly include a margin of error (±) are considered as well-constrained and reasonably accurate (Stock et al., 2013).

Rockfall date	Measured volume (m³) from SfM-TLS	Reported volume (m³) from the inventory database	Volume difference (m³) (%)	
3 Oct. 1976 (EC)	1864 ± 481 (S)	510	− 1354	− 73
10 Mar. 1987 (MB)	20,193 ± 2957 (R)	*600,000*	+ 579,807	+ 97
Feb. 1992 (EC)	93 ± 37 (T)	150 ± 50	+ 57	+ 38
Mar. 1993 (EC)	2019 ± 342 (C)	900 ± 300	− 1119	− 55
22 Feb. 2000 (MB) (2 events)	9534 ± 1236 (T) 4774 ± 715 (T)	17,477	+ 3169	+ 18
1 Mar. 2000 (MB)	17,304 ± 2391 (C)	21,747	+ 4443	+ 20
11 Oct. 2010 (EC)	653 ± 173 (C)	990	+ 337	+ 34

Table 2
Characteristics of rockfall volume-frequency distributions for the two study sites. Key to abbreviations: EC = El Capitan; MB = Middle Brother; SSE = Sum of Squared estimate of Errors; RMSE = Root Mean Square Error. V_{obs} is the range of observed volumes; V_0, the value of minimum volume used for power law fit; N_{fit}, the number of events used for power law fit; b, the maximum likelihood estimate of b value. The right-hand columns (R^2, SSE and RMSE) give the values obtained when the power laws are extrapolated up to the maximum listed volumes.

Site	Period	Data set	N_{events}	V_{obs} (m^3)	V_0 (m^3)	N_{fit}	b	R^2		SSE		RMSE	
EC	1976	database	38	10^{-1}–10^4	27	15	0.41 ± 0.11	0.98	0.96	0.17	0.61	0.10	0.17
	2017	SfM-TLS	115	10^{-2}–10^4	0.24	70	0.39 ± 0.05	0.99	0.98	0.13	1.01	0.04	0.11
MB	1976	database	54	1–6.10^5	0.06	39	0.36 ± 0.06	0.96	0.96	0.24	1.29	0.08	0.16
	2016	SfM-TLS	120	10^{-2}–2.10^4	4	81	0.32 ± 0.04	0.99	0.98	0.09	1.59	0.03	0.13

Capitan and Middle Brother, as well as other locations), it is necessary to use spatio-temporal rockfall frequencies (Hantz, 2011; Barlow et al., 2012), which represent the number of rockfalls per unit time and per unit area. It should be noted that only the *a*-value changes during the conversion to the spatio-temporal domain; the *b*-value remains unchanged. We divided the number of rockfalls from each inventory by the number of years of monitoring and by the cliff surface areas expressed in km^2. Thus, the values of *a* reported in Section 4.4 and Fig. 9 correspond to numbers of rockfalls (larger than 1 m^3) per year and per km^2.

4. Results and discussion

4.1. Measured versus reported number of rockfalls

Our SfM-TLS analyses detected 235 rockfall from the southeast faces of El Capitan and Middle Brother. For El Capitan, we detected 115 rockfalls between 1976 and 2017 (Fig. 6A). The majority of these rockfalls are concentrated in two areas: a 1976–1993 (Fig. 6B) scar area and a 2010–2017 scar area (Fig. 6C). The 2010–2017 scar area has been the more active of the two, with two-thirds of all rockfalls (70 in total) located in this area (Fig. 6C). The spatial and temporal progression of the 2010–2017 rockfall sequence shows that rockfalls generally propagated upward and outward from the location of the first event (Stock et al., 2018). A similar rockfall progression was documented at the Rhombus Wall (Stock et al., 2012), located 5 km east of El Capitan, linking the progression to rockfall-induced redistribution of stresses on the cliff, which can incite propagation of microfractures (Petley et al., 2005) and/or failure of rock bridges (Kemeny, 2005). The 1976–1993 scar area has apparently been less active, although we note that

both the inventory database and the SfM-TLS analyses here are subject to bias; both are subject to underreporting of small rockfalls, as well as the effects of superimposition and/or coalescence.

SfM-TLS analyses detected 120 rockfalls from the southeast face of Middle Brother between 1976 and 2016 (Fig. 8A). Unlike El Capitan, there is no preferential location for rockfalls on Middle Brother, although three consecutive large rockfalls in February and March 2000 are located close to each other (Figs. 7 and 8A). Similar to the 2010–2017 rockfalls from El Capitan, a lateral progression of five adjacent rockfalls was observed from the southeast face of Middle Brother between October 2015 and August 2016 (Fig. 8C). In addition, it is interesting to note that the first and largest event of this sequence (2844 m^3) was preceded by a series of small rockfalls (7 events of 4 m^3 on average) in 2013–2015, located immediately adjacent to the future scar (Fig. 8C). Anecdotally, small rockfalls also preceded the 10 March 1987 Middle Brother rockfall (Stock et al., 2013), but with only two datasets (1976 SfM and 2010 TLS) bracketing the event we are not able to quantify those events in space or time. The ongoing rockfall activity at specific locations is consistent with the broader observation, well-documented in the inventory database, that rockfall scars in Yosemite are commonly active over years to decades. This is indicative of the sporadic nature of rockfalls in both space and time, and highlights the effects of superimposition and coalescence. However, there are significant exceptions; for example, two adjacent rockfall scars from March 2000 display markedly different activity after the scar-forming event, with 18 rockfalls (minimum value due to the biases mentioned above) detected within the western scar between 2010 and 2016, but no rockfalls (minimum value) detected within the eastern scar over the same period (Fig. 8B).

The more thorough accounting of rockfalls provided by the SfM-TLS measurements allows us to assess the observation bias that affects the
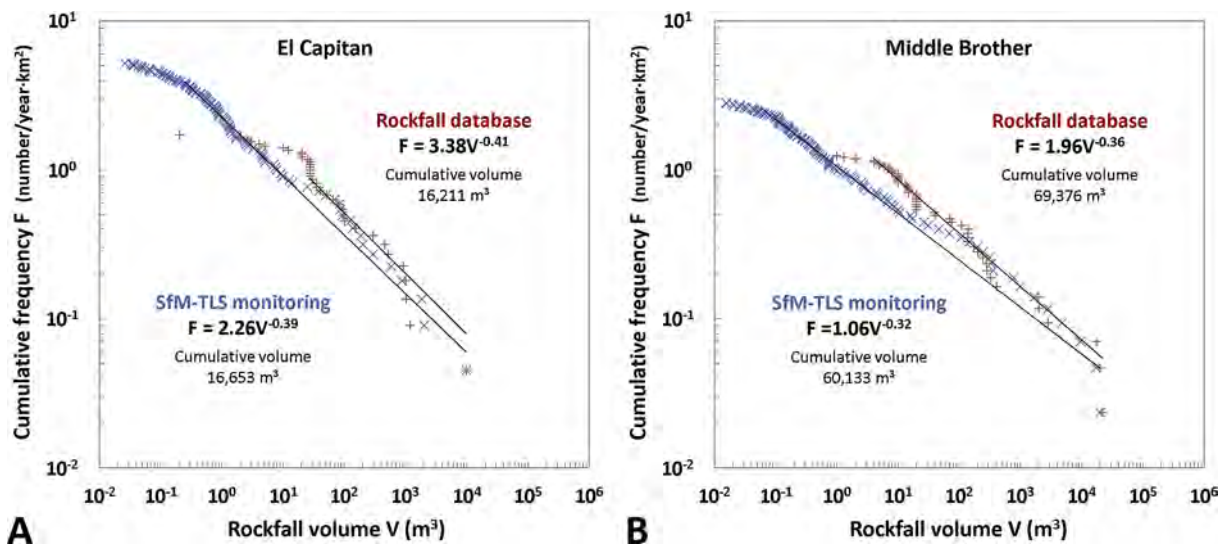

Fig. 9. Rockfall volume-frequency relationships for the SE faces of El Capitan and Middle Brother between 1976 and 2016–2017. **(A)** and **(B)** Red data points are from the Yosemite rockfall inventory database (Stock et al., 2013) and subsequent observations; blue data points are from SfM-TLS monitoring. The four cumulative spatio-temporal distributions were fitted with power laws using the maximum likelihood method (Aki, 1965; Dussauge et al., 2003; Clauset et al., 2009); the domains of validity and goodness-of-fit parameters of each curve are specified in Table 2. (For interpretation of the references to color in this figure legend, the reader is referred to the web version of this article.)
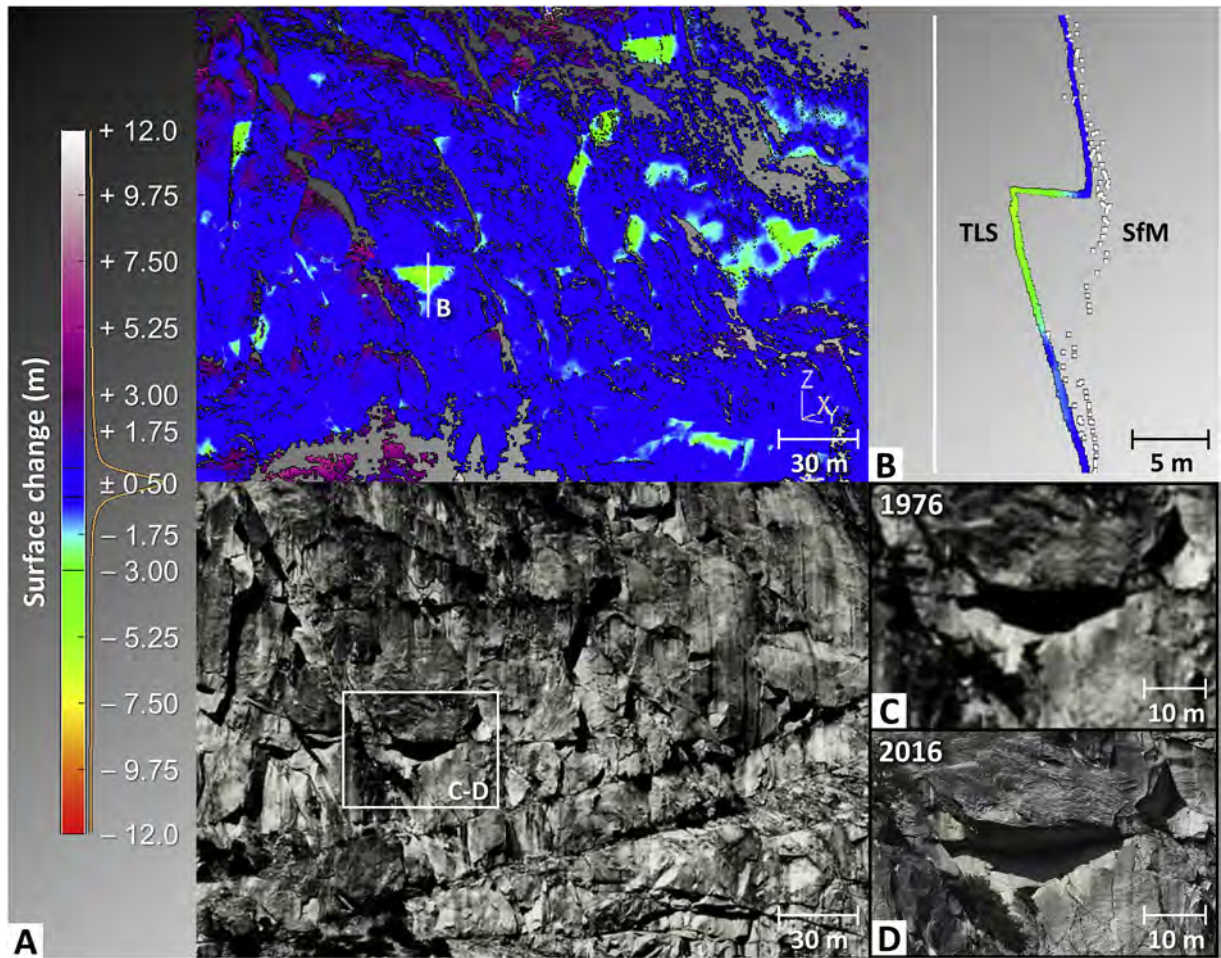
Fig. 10. Artifacts (false rockfalls) induced by the presence of shadows in the 1976 photographs. **(A)** Filtered point-to-mesh differences between the 1976 SfM point cloud and the 2010 TLS mesh (upper panel; Middle Brother; extract from Fig. 7) and front view of the corresponding area in 1976 (lower panel). The extract corresponds to the cliff section located above the rockfall scars of Feb.-Mar. 2000 (Fig. 7). **(B)** Profile view of cross-section P annotated in Panel A. The negative deviations observed within the overhang are due to poor reconstruction of the SfM points in the shadowed area. **(C)** and **(D)** Before-after comparison of the area framed in Panel C; cross-section P is located in the middle of the overhang. Visual inspection confirms the "false rockfall" artifact.

inventory database. Still, due to the infrequent monitoring interval of TLS data (1.5 year in average), it should be specified that the number of rockfalls detected and their individual volumes are both potentially subject to the effects of superimposition and coalescence. When monitoring intervals exceed rockfall return periods, superimposed or amalgamated rockfalls are recorded as single detachments, with the result that multiple smaller rockfalls may be recorded as a single larger rockfall (Williams et al., 2019). In addition, the average resolution of TLS data (<250 pts/m^2), as well as the resolution decrease with distance from the TLS scanner to the cliff, limits the detection of events below 0.02 m^3, especially in the upper part of the cliffs. Thus, it is likely that the number of small rockfalls involved in the 2010–2016 period is strongly underestimated. Here, recording of rockfalls in the inventory database can help to evaluate whether superimposition and/or coalescence are substantially affecting the number and volumes of rockfalls detected by the SfM-TLS analyses. In terms of number of events, the observer bias is substantial. For El Capitan, the inventory database documents 38 rockfalls between 1976 and 2017, compared to 115 rockfalls detected by SfM-TLS (Fig. 6). For Middle Brother, the inventory database records 54 rockfalls between 1976 and 2016, compared to 120 rockfalls detected by SfM-TLS (Fig. 8). Both cases suggest that the inventory database documents less than half of the rockfalls detected by SfM-TLS. For both cliffs, the majority of rockfalls not reported in the inventory database are small in volume (<1 m^3), which likely explains the under-

reporting, as such small rockfalls often are not observed and therefore not recorded.

4.2. Measured versus reported rockfall volumes

The SfM-TLS measurements also allow us to assess how accurately the inventory database records both individual and cumulative rockfall volumes. The representative sample of the eight rockfalls (four for El Capitan and four for Middle Brother) highlighted in Figs. 4 and 7 provides a sufficiently wide range of volumes and time periods to assess the accuracy and precision of the volume estimates reported in the inventory database. Chronologically, the comparison of reported and measured volumes shows that three-quarters of the volumes for these eight events were originally overestimated (Table 1). On average, volumes were overestimated by a factor of 1.4 but in one case (the 10 March 1987 Middle Brother rockfall event, discussed in more detail below), the overestimation was by a factor of nearly 30. Overall, reported rockfall volumes become increasingly accurate over time, with an error range less than a factor of 1.5 since the late 1990s (Table 1). This is due to a more concerted effort to accurately estimate volumes, as well as the increasing availability of aerial and terrestrial lidar data, which allow more accurate measurements of rockfall scar dimensions. Over the time period 2010–2017, this trend is broadly confirmed; for example, the 11 June 2014 El Capitan rockfall (977 m^3; Fig. 6A) was
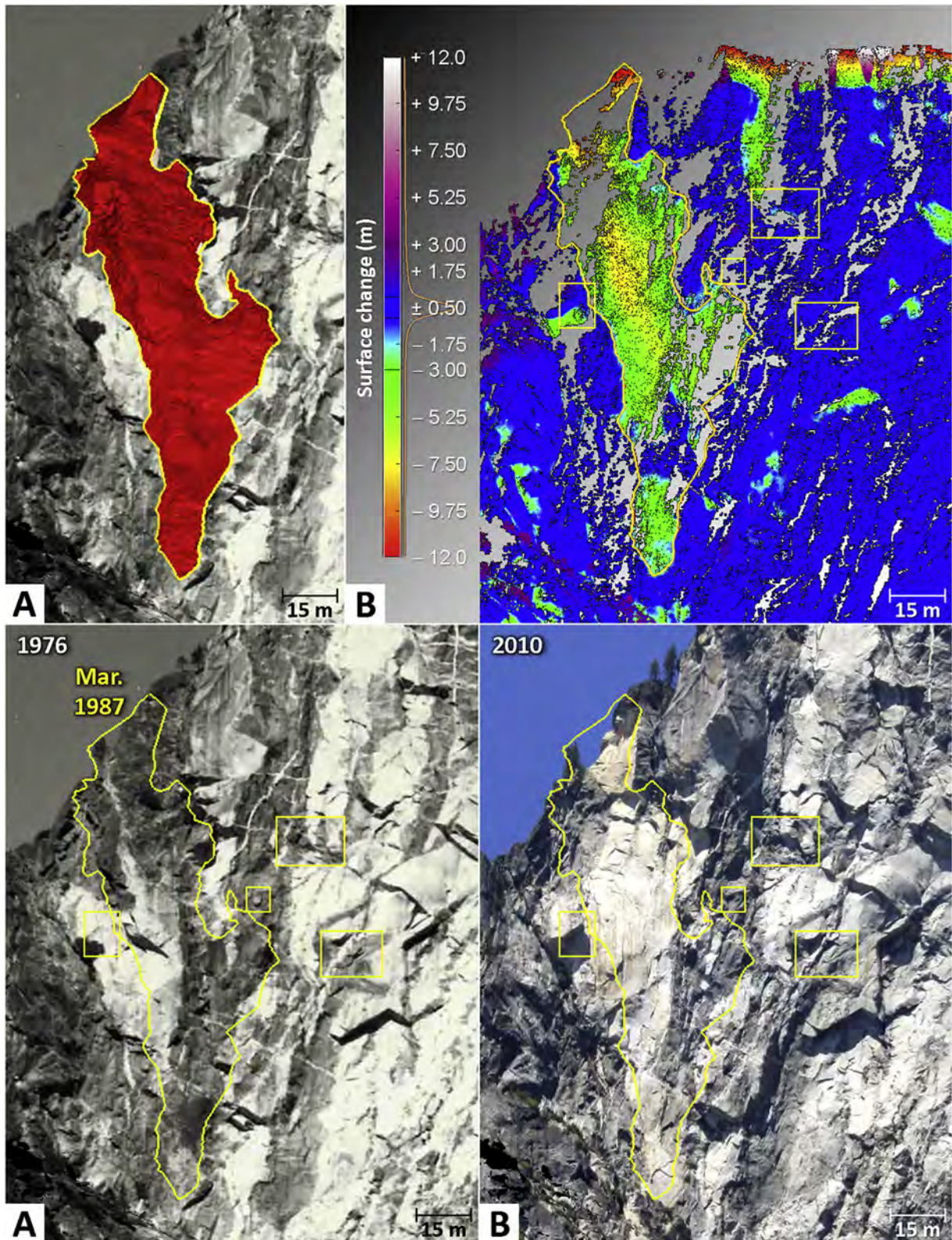
Fig. 11. Detailed analysis of the surface changes detected within the 10 Mar. 1987 rockfall scar on Middle Brother. **(A)** Pre-event topographic surface (red triangular mesh) and lateral boundaries (yellow polyline) of the rockfall. Background image: photograph shown in Panel C. **(B)** Filtered point-to-mesh differences between the 1976 SfM point cloud and the 2010 TLS mesh (extract from Fig. 7). Rectangles indicate the location of 4 rockfalls that were not detected by SfM-TLS analyses. This finding highlights the limitations of the historical SfM to detect small rockfalls, as the left-most rectangle has been associated with the artifact highlighted in Fig. 10 and the other three rectangles contained too few, if any, negative deviations situated outside the change detection uncertainty to be considered as true rockfalls. **(C)** and **(D)** Before-after comparison of the area shown in Panel B; visual inspection confirms the occurrence of small rockfalls in these locations. (For interpretation of the references to color in this figure legend, the reader is referred to the web version of this article.)

estimated at 450 m^3, and the 1 October 2015 Middle Brother rockfall (46 m^3; Fig. 8A) was estimated at 75 m^3.

4.2.1. Volume of the 10 March 1987 rockfall

The largest volume discrepancy identified between the inventory database and the SfM-TLS analyses involves the 10 March 1987 Middle Brother rockfall. According to the inventory database, this was the largest historical rockfall in Yosemite Valley (since 1857), at 600,000 m^3. Based on the combined SfM-TLS analyses, we measured a volume for this rockfall of 20,193 m^3, which contrasts strongly with the previously reported estimate. The 10 March 1987 rockfall was carefully observed by park rangers, primarily because it was preceded by many small rockfalls that led to closure of a major road corridor prior to the largest rockfall occurring (Stock et al., 2013). Immediately after the largest rockfall, a rapid assessment of the rockfall source area approximately outlined the extent and offered rough dimensions of width, height, and thickness of the failed rock mass (James Snyder, pers. comm., 2019). These dimensions were the basis for the 600,000 m^3 volume estimate, which was then cited in subsequent publications (Wieczorek, 2002; Wieczorek and Snyder, 2004; Wieczorek et al., 1992, 1995; Stock et al., 2013) without a detailed analysis. Although the estimated extent of the rockfall scar as shown in Wieczorek (2002) closely matches our measured extent (Fig. 11), the point cloud data show that the each of the dimensions were overestimated, leading to a substantial cumulative overestimation of the volume.

Several lines of field evidence further support the smaller volume for the 10 March 1987 rockfall measured by SfM-TLS. First, debris from this rockfall traveled only slightly beyond the base of the talus slope beneath Middle Brother, whereas elsewhere in Yosemite Valley prehistoric rockfalls with volumes exceeding 500,000 m^3 extended hundreds of meters beyond the base of talus slopes, spreading out over the valley floor (Wieczorek et al., 1999; Stock and Uhrhammer, 2010). Second, photographs of the talus slope beneath Middle Brother taken before and after the rockfall do not show the magnitude of change that would be expected from a rockfall exceeding 500,000 m^3. We conclude that the smaller volume of approximately 20,200 m^3 for the 10 March 1987 Middle Brother rockfall is accurate, and use this opportunity to correct the record.

4.2.2. Cumulative rockfall volumes

The cumulative rockfall volume measured by SfM-TLS from El Capitan between 1976 and 2017 is 16,653 m^3 (Fig. 9A). Over the same time period, the inventory database reports a cumulative volume of 16,211 m^3 (Fig. 9A), in close agreement with the volume measured by SfM-TLS. In contrast, the measured cumulative volume for rockfalls from Middle Brother between 1976 and 2016 is 60,133 m^3 (Fig. 9B), whereas over the same time period the inventory database records a cumulative volume of 649,183 m^3, more than an order-of-magnitude larger than the measured volume. This discrepancy is almost entirely due to the overestimation of the 10 March 1987 rockfall volume described above. When the incorrect estimated volume for this event (600,000 m^3) is corrected to the measured volume (20,193 m^3), the cumulative volume from the inventory database is 69,376 m^3 (Fig. 9B), bringing the measured and estimated volumes into much closer alignment. Thus, although the inventory database suffers from an underreporting of rockfalls (it records substantially fewer rockfalls than detected by SfM-TLS), its accuracy improves in recording cumulative rockfall volumes. This is likely because the large-volume rockfalls that contribute most to the cumulative volume tend not to escape observation, as they are loud, often produce highly-visible dust clouds, and are more likely to block roads or trails or otherwise disrupt park operations. As such, these events typically receive more study and their volumes are more carefully estimated (with the notable exception of the 10 March 1987 Middle Brother rockfall). In addition, unlike the number of detected rockfalls, the cumulative eroded volume detected with TLS or SfM is not affected by superimposition or coalescence. Thus, as is the case with landslides (e.g., Malamud et al., 2004;

Galli et al., 2008; Brunetti et al., 2009; Tanyaş et al., 2017), it is often more representative to use the cumulative eroded surfaces/volumes rather than the number of events to compare inventories.

With greater confidence in the measured volumes, we can quantify differences in cumulative volume between the two cliffs. Over a 41-year-period, El Capitan lost 16,653 m^3 of rock, whereas over a 40-year period, Middle Brother lost 60,133 m^3 of rock, nearly four times more than El Capitan. As the number of rockfalls from both cliffs is similar (115 for El Capitan and 120 for Middle Brother), the discrepancy is due to the larger volumes of many of the rockfalls from Middle Brother. All other factors (e.g., rock mass properties) being equal, cumulative rockfall volume should scale with cliff area (i.e., a larger cliff area has greater potential for a rockfall of a given volume), so a meaningful volumetric comparison requires accounting for cliff area, resulting in a measure of cliff retreat over time (Moore et al., 2009). The cliff surface area of the southeast face of El Capitan is roughly half that of the southeast face of Middle Brother (537,820 m^2 and 1,063,600 m^2, respectively). However, the morphology of these two cliffs is very different, with a slightly overhanging circular arc for the southeast face of El Capitan versus a step-path geometry for the southeast face of Middle Brother (Fig. 1). Thus, to limit the consideration of very low dip areas (<20°) that are not likely to produce rockfalls, we projected the TLS meshes orthogonally onto the average plane of each cliff, resulting in projected cliff surface areas of 471,100 m^2 and 901,610 m^2, respectively. Even after accounting for cliff surface area, the larger volume loss from Middle Brother (now per km^2) persists, indicating greater rockfall activity and volume loss from that cliff compared to El Capitan.

4.3. Spatio-temporal rockfall frequencies

Volume-frequency relationships for Yosemite rockfalls were previously evaluated over the period 1900–1992 using a catalogue of 214 events (Wieczorek et al., 1995), then subsequently over the period 1915–1992 using only the volume estimates constrained field observations (catalogue of 101 events, Dussauge-Peisser et al., 2002) and finally over the period 1857–2002 using a catalogue of 392 events (Guzzetti et al., 2003). These three cumulative distributions are quite well described by power-law relationships (R^2 > 0.97) with b exponents (Eq. (1)) equal to 0.57, 0.46 and 0.40, respectively. However, it should be noted that the power-law modeled by Guzzetti et al. (2003) only concerns the period 1980–2002, considered as reasonably complete in terms of inventory. These three distributions are also characterized by a rollover (flattening of the curve) of volume-frequency for rockfall volumes <300 m^3 (Wieczorek et al., 1995) and 50 m^3 (Dussauge-Peisser et al., 2002; Guzzetti et al., 2003), respectively. In most historical inventories, the rollover of the small volumes is attributable to observation bias (undersampling) (Hungr et al., 1999; Stark and Hovius, 2001; Malamud et al., 2004; Brunetti et al., 2009).

The SfM-TLS derived spatio-temporal rockfall frequencies obtained for El Capitan and Middle Brother (Fig. 9) over the period 1976–2017 are very well fitted (Table 2) (R^2 > 0.99; SSE < 0.15; RMSE<0.05) by power-law relationships between 0.2 m^3 and 25 m^3 (70 events) and between 0.05 m^3 and 20 m^3 (81 events), respectively. Beyond 20 m^3, the correlation coefficient remains high (R^2 > 0.98) but the other goodness-of-fit indicators become significantly higher, with SSE values >1 and RMSE values >0.1 (Table 2). As in many studies (e.g., Hungr et al., 2008; Dewez et al., 2013; Strunden et al., 2015), this difference is due to the small number of large volume events that occurred during our observation period (Fig. 9); this is the censoring effect described by Stark and Hovius (2001). Regarding the spatio-temporal rockfall frequencies associated with the inventory database, the goodness-of-fit indicators are satisfactory (Table 2) (R2 > 0.96; SSE < 0.25; RMSE < 0.10) between 25 m^3 and 1000 m^3 (15 events) for El Capitan and between 2 m^3 and 300 m^3 (39 events) for Middle Brother. These lower values are attributable to the method, mentioned in the introduction, of assigning estimated volumes to the inventory database, which generates an uneven distribution

characterized by frequency jumps at volumes of 20 m³, 200 m³, 2000 m³ and 20,000 m³ (Fig. 9). These jumps were already visible in the previous studies of the Yosemite rockfall inventory database (Dussauge-Peisser et al., 2002; Guzzetti et al., 2003). The under-sampling effect also affects the distribution of small rockfall volumes, with a rollover visible on the four volume-frequency relationships. The rollover position is between 2 m³ and 25 m³ for the rockfall database (Fig. 9) and between 0.05 m³ and 0.2 m³ for the SfM-TLS monitoring (Fig. 9). This shift arose because the 2010–2017 monitoring allowed the detection of many rockfalls smaller than 10 m³ (about 80% of the total number of rockfalls in both SfM-TLS inventories).

The slope (given by the b-value) of the spatio-temporal rockfall frequencies varies between 0.39 (SfM-TLS) and 0.41 (inventory database) for El Capitan and between 0.32 (SfM-TLS) and 0.36 (inventory database) for Middle Brother (Fig. 9). These values are slightly lower than both exponents highlighted by Dussauge-Peisser et al. (2002) and Guzzetti et al. (2003). The small discrepancy with the previous studies can be explained first by the fact that the time periods evaluated by the various studies are not the same (more recent time periods have a more thorough accounting of rockfalls), and, second, because both above-mentioned studies use data from all of Yosemite Valley and not just that from El Capitan and Middle Brother as we do here. Additionally, the number of small rockfalls remains under-represented in the SfM-TLS analyses, as shown by the lack of detected rockfalls smaller than 1 m³ between 1976 and 2010. This under-representation of small volumes affects the b-value associated with the SfM-TLS analyses, which would probably have been slightly higher with a larger number of small rockfalls (Williams et al., 2019). Despite these uncertainties, all the b-values are well below 1, indicating that the contribution of large volumes is significantly higher than that of small volumes for the erosion of granitic cliffs in Yosemite Valley. Fig. 9 also shows that the slope of the spatio-temporal rockfall frequencies is higher for the inventory database. This difference highlights the importance of having the most accurate volume estimates possible (e.g., the overestimation of the 10 March 1987 rockfall volume) and for monitoring with a high spatio-temporal resolution in order to derive more reliable volume-frequency relationships.

The spatio-temporal rockfall activity, given by the a-value, appears twice as high for El Capitan than for Middle Brother; on average, 2.3 rockfalls from El Capitan (compared to 1.1 from Middle Brother) larger than 1 m³ (when considering V = 1 m³ in Eq. (1)) have occurred per year and per km² of cliff between 1976 and 2017 (Fig. 9). This difference in behavior can be explained by the fact that there were as many detected rockfalls over virtually the same time period from a cliff with half of the surface area. Still, the 2017 El Capitan rockfall sequence strongly influenced the a-value, as almost half of the inventory (51 out of 115 events) was recorded in the short time period between September and November 2017. This result indicates that the rockfall frequencies of El Capitan and Middle Brother were actually similar until the end of 2016, even though larger volumes had affected the southeast face of Middle Brother since 1987.

Although our 40-year monitoring period is longer than that most other similar studies, it is still too short to accurately estimate the return periods associated with the largest-volume rockfalls. In addition, due to biases and uncertainties discussed earlier, return periods should be considered approximate. Nevertheless, it is interesting to note that for the specific cliffs of El Capitan and Middle Brother, the SfM-TLS spatio-temporal rockfall frequencies provide a return period between 50 and 100 years for an event similar in volume to the 28 September 2017 El Capitan rockfall (9811 m³) (Fig. 9A). By way of comparison, the return period of this same event drops to around six years when considering all cliffs in Yosemite Valley (Stock et al., 2018). For events similar to the 1 March 2000 (17,304 m³) and 10 March 1987 (20,193 m³) Middle Brother rockfalls, the return period is between 65 and 100 years (Fig. 9B). For the entire Yosemite Valley, this return period (for the largest volume) is approximately 16 years. Defining rockfall frequency is

essential for characterizing rockfall hazard, and determining even approximate return periods can help park managers in Yosemite place large rockfalls into context.

4.4. Cliff retreat rates

The cumulative volumes and projected cliff surface areas obtained from the SfM-TLS data allow us to calculate spatially and temporally averaged cliff retreat rates. The cliff retreat rate of El Capitan (1976–2017) is 0.86 mm/yr. The cliff retreat rate for Middle Brother (1976–2016) is 1.67 mm/yr. Thus, even when the larger cliff area of Middle Brother is accounted for, its retreat rate is nearly twice as fast as that for El Capitan, indicating a substantial difference in rockfall activity between the two cliffs over that 40-year period. The cliff retreat rates we measure for El Capitan and Middle Brother are faster than cliff retreat rates measured in alpine areas of the Sierra Nevada (average of 0.3 mm/yr; Moore et al., 2009), and much faster than other surface process rates measured in the range (e.g., river incision rates of 0.02–0.3 mm/yr and bare bedrock erosion rates of 0.01 mm/yr; Stock et al., 2005, and references therein). This confirms that rockfalls are the dominant geomorphic process presently acting in Yosemite Valley. Cliff retreat rates for El Capitan and Middle Brother are also generally faster than cliff retreat rates measured in other mountainous settings, which typically vary from 0.1 to 1.0 mm/yr (e.g., Moore et al., 2009; Strunden et al., 2015, and references therein). The faster cliff retreat rates in Yosemite Valley likely result from unique geological and climatological factors, in particular the continuously exfoliating nature of the exceptionally steep granitic cliffs, as well as the multitude of potential triggering mechanisms (Stock et al., 2013). However, caution should be exercised when comparing retreat rates derived from different time scales of observation. Although the cliff retreat rates we report here are derived from four decades of observation (a length of time much greater than most studies), this is potentially still a short period of observation relative to the frequency of larger-volume rockfalls.

The sensitivity of the time scale of observation is illustrated by comparing cumulative volumes from El Capitan over a 40-year-period (1976 to 2016, the same time interval over which we evaluate Middle Brother) versus a 41-year period (1976 to 2017, enabled by additional SfM acquisitions for El Capitan in 2017; Stock et al., 2018). If the analysis of El Capitan were limited to 1976–2016, the cumulative volume would be 5723 m³, yielding a cliff retreat rate of 0.58 mm/yr. However, if the analysis is expanded by just one year to 1976–2017, the cumulative volume is 10,921 m³, yielding the cliff retreat rate of 0.86 mm/yr reported above. This highlights the sensitivity of the time scale of observation, especially when cumulative volumes are substantially affected by individual large-volume rockfalls.

To evaluate whether the cliff retreat rates we measure over four decades are indicative of longer term rates, we followed the method described by Barlow et al. (2012) for calculating the long-term averaged total eroded volumes from modeled volume-frequency power laws. This method consists of multiplying the frequency density of rockfall volumes by the volume V, then integrating it between a minimum and maximum volume. Considering a minimum volume of 10^{-3} m³ and a maximum volume of 10^5 m³, we determine a total eroded volume of 89,400 m³ for El Capitan and 133,300 m³ for Middle Brother, corresponding to long-term cliff retreat rates of 1.66 mm/yr and 1.25 mm/yr, respectively. Although these results are sensitive to the choice of the maximum volume (e.g., changing the maximum volume to 10^6 m³ increases those rates to 6.70 mm/yr and 6.02 mm/yr, respectively), within a realistic range of rockfall volumes it appears that the cliff retreat rates we derive from TLS-SfM are indicative of longer-term rates.

5. Conclusions

Integrating terrain models derived from TLS and modern SfM with models derived from SfM of "historical" (archival) imagery can substantially extend detections of landscape change back in time. Historical oblique photographs taken of the southeast faces of El Capitan and

Middle Brother in Yosemite Valley yielded high-resolution terrain models of those cliffs as they appeared in 1976. By differencing those earlier terrain models against more recent models derived from TLS and SfM, we detected 235 rockfalls from the two cliffs over a 40-year period. We find that although the number of rockfalls detected from the two cliffs is similar, Middle Brother has lost a substantially larger volume of rock, with a correspondingly higher cliff retreat rate. A rockfall inventory database for Yosemite records roughly half the number of rockfalls detected by TLS-SfM, although most of the unrecorded rockfalls are <1 m^3 in volume, suggesting that they were too small to be noticed and therefore not reported. Individual rockfall volumes reported in the inventory database vary from those measured by TLS-SfM, with reported volumes most often overestimated. However, cumulative volumes over the 40-year period are similar between the inventory database and the TLS-SfM analyses, likely because large volume rockfalls tend not to escape notice. Improved volume-frequency relationships confirm that infrequent large volume rockfalls contribute more to cliff erosion in Yosemite Valley than more frequent small volume rockfalls. Rates of cliff retreat for El Capitan and Middle Brother are much faster than other surface process rates in the Sierra Nevada, and are generally faster than cliff retreat rates measured in other mountainous settings. The high fidelity of TLS and SfM techniques, combined with the ability to generate SfM-based terrain models of cliffs as they appeared decades ago, allows unprecedented opportunities to detect rockfall activity, measure rockfall volumes, assess rockfall hazard, and quantify rates of cliff retreat in mountainous landscapes.

Despite the small number of photographs (<25), originally unintended for SfM photogrammetry, a non-constant overlapping (ranging between 20 and 70%), and variable lighting conditions, our method turns out to be sufficiently accurate and consistent with the inventory database to reassess volumes ranging from a few tens to several tens of thousands of cubic meters. In the context of improving our understanding of landscape evolution, this finding opens up new perspectives for using historical (archival) photographs by obtaining new volume estimates of historical events (rockfalls, rockslides, debris flows, etc.) and more precisely quantifying other types of surface processes.

Supplementary data to this article can be found online at https://doi.org/10.1016/j.geomorph.2020.107069.

Declaration of competing interest

The authors declare that they have no known competing financial interests or personal relationships that could have appeared to influence the work reported in this paper.

Acknowledgements

Author contributions statement

A.G., G.M.S., M.J. and B.D.C. devised the study. A.G., G.M.S., M.J. and B.M. collected the TLS data. G.M.S. and N.A. collected the 2017 SfM data. A.G. processed all the data. A.G., G.M.S., M.J.R., M.J. and B.D.C. analyzed and interpreted the results. A.G. and G.M.S. wrote the paper with input from M.J.R., M.J., B.D.C., B.M., N.A. and M.-H.D.

Data availability

The datasets generated during and/or analyzed during the current study are available from the corresponding author on reasonable request.

References

Abellán, A., Jaboyedoff, M., Oppikofer, T., Vilaplana, J.M., 2009. Detection of millimetric deformation using a terrestrial laser scanner: experiment and application to a rockfall event. Nat. Hazards Earth Syst. Sci. 9 (2), 365–372.

Abellán, A., Calvet, J., Vilaplana, J.M., Blanchard, J., 2010. Detection and spatial prediction of rockfalls by means of terrestrial laser scanner monitoring. Geomorphology 119 (3–4), 162–171.

Agisoft (2014): Agisoft PhotoScan Professional edition Software (version 1.0.4). Agisoft LLC. Available from: https://www.agisoft.com/downloads/installer/

Aki, K., 1965. Maximum likelihood estimate of b in the formula log N= a-bM and its confidence limits. Bull. Earthq. Res. Inst., Tokyo Univ. 43, 237–239.

Bahat, D., Grossenbacher, K., Karasaki, K., 1999. Mechanism of exfoliation joint formation in granitic rocks, Yosemite National Park. J. Struct. Geol. 21 (1), 85–96.

Bakker, M., Lane, S.N., 2017. Archival photogrammetric analysis of river–floodplain systems using Structure from Motion (SfM) methods. Earth Surf. Process. Landf. 42 (8), 1274–1286.

Barlow, J., Lim, M., Rosser, N., Petley, D., Brain, M., Norman, E., Geer, M., 2012. Modeling cliff erosion using negative power law scaling of rockfalls. Geomorphology 139-140, 416–424.

Bateman, P.C. (1992): Plutonism in the Central Part of the Sierra Nevada Batholith, California. U.S. Geological Survey Professional Paper 1483, 186 p.

Besl, P.J., McKay, N.D., 1992. A method for registration of 3-D shapes. IEEE Trans. Pattern Anal. Mach. Intell. 14 (2), 239–256.

Brunetti, M.T., Guzzetti, F., Rossi, M., 2009. Probability distributions of landslide volumes. Nonlinear Process. Geophys. 16 (2), 179–188.

Budetta, P., Nappi, M., 2013. Comparison between qualitative rockfall risk rating systems for a road affected by high traffic intensity. Nat. Hazards Earth Syst. Sci. 13 (6), 1643–1653.

Byers, S., Raftery, A.E., 1998. Nearest-neighbor clutter removal for estimating features in spatial point processes. J. Am. Stat. Assoc. 93 (442), 577–584.

Calkins, F.C., Huber, N.K., and Roller, J.A. (1985): Geologic bedrock map of Yosemite Valley, Yosemite National Park, California. U.S. Geological Survey Miscellaneous Investigations Series Map I–1639.

Carrea, D., Abellan, A., Derron, M.-H., & Jaboyedoff, M. (2015): Automatic rockfalls volume estimation based on terrestrial laser scanning data. In Engineering Geology for Society and Territory-volume 2 (pp. 425-428). Springer, Cham.

Chau, K.T., Wong, R.H.C., Liu, J., Lee, C.F., 2003. Rockfall hazard analysis for Hong Kong based on rockfall inventory. Rock Mech. Rock. Eng. 36 (5), 383–408.

Chen, Y., Medioni, G., 1992. Object modelling by registration of multiple range images. Image Vis. Comput. 10 (3), 145–155.

Clauset, A., Shalizi, C.R., Newman, M.E., 2009. Power-law distributions in empirical data. Society for Industrial and Applied Mathematics review 51 (4), 661–703.

Copons, R., Vilaplana, J.M., 2008. Rockfall susceptibility zoning at a large scale: from geomorphological inventory to preliminary land use planning. Eng. Geol. 102 (3–4), 142–151.

Corominas, J., Moya, J., 2008. A review of assessing landslide frequency for hazard zoning purposes. Eng. Geol. 102 (3–4), 193–213.

De Biagi, V., Napoli, M.L., Barbero, M., Peila, D., 2017. Estimation of the return period of rockfall blocks according to their size. Nat. Hazards Earth Syst. Sci. 17 (1), 103–113.

Delonca, A., Gunzburger, Y., Verdel, T., 2014. Statistical correlation between meteorological and rockfall databases. Nat. Hazards Earth Syst. Sci. 14 (8), 1953–1964.

Derrien, A., Villeneuve, N., Peltier, A., Beauducel, F., 2015. Retrieving 65 years of volcano summit deformation from multitemporal structure from motion: the case of Piton de la Fournaise (La Réunion Island). Geophys. Res. Lett. 42 (17), 6959–6966.

Dewez, T.J.B., Rohmer, J., Regard, V., Cnudde, C., 2013. Probabilistic coastal cliff collapse hazard from repeated terrestrial laser surveys: case study from Mesnil Val (Normandy, northern France). J. Coast. Res. 65 (sp1), 702–707.

Douglas, G.R., 1980. Magnitude frequency study of rockfall in Co. Antrim, N. Ireland. Earth Surface Processes 5 (2), 123–129.

Dunham, L., Wartman, J., Olsen, M.J., O'Banion, M., Cunningham, K., 2017. Rockfall Activity Index (RAI): a lidar-derived, morphology-based method for hazard assessment. Eng. Geol. 221, 184–192.

Dussauge, C., Grasso, J.R., Helmstetter, A., 2003. Statistical analysis of rockfall volume distributions: Implications for rockfall dynamics. J. Geophys. Res. 108 (B6), 2286.

Dussauge-Peisser, C., Helmstetter, A., Grasso, J.R., Hantz, D., Desvarreux, P., Jeannin, M., Giraud, A., 2002. Probabilistic approach to rock fall hazard assessment: potential of historical data analysis. Nat. Hazards Earth Syst. Sci. 2 (1/2), 15–26.

Eltner, A., Kaiser, A., Castillo, C., Rock, G., Neugirg, F., Abellán, A., 2016. Image-based surface reconstruction in geomorphometry–merits, limits and developments. Earth Surface Dynamics 4 (2), 359–389.

Esposito, G., Salvini, R., Matano, F., Sacchi, M., Troise, C., 2018. Evaluation of geomorphic changes and retreat rates of a coastal pyroclastic cliff in the Campi Flegrei volcanic district, Southern Italy. J. Coast. Conserv. 22 (5), 957–972.

Ester, M., Kriegel, H.P., Sander, J., Xu, X., 1996. A density-based algorithm for discovering clusters in large spatial databases with noise. In: Proceedings of the 2nd International Conference on Knowledge Discovery and Data Mining, Portland, Oregon, 96(34), pp. 226–231.

Galli, M., Ardizzone, F., Cardinali, M., Guzzetti, F., Reichenbach, P., 2008. Comparing landslide inventory maps. Geomorphology 94 (3–4), 268–289.

Gardner, J., 1970. Rockfall: a geomorphic process in high mountain terrain. Albertan Geographer 6, 15–20.

Gardner, J., 1983. Rockfall frequency and distribution in the Highwood Pass area, Canadian Rocky Mountains. Zeitshrift fur Geomorphologie, NF 27, 311–324.

Gilham, J., Barlow, J., Moore, R., 2019. Detection and analysis of mass wasting events in chalk sea cliffs using UAV photogrammetry. Eng. Geol. 250, 101–112.

Girardeau-Montaut, D. (2015): CloudCompare (version 2.7.0). [GPL software], EDF RandD, Telecom ParisTech. Available from: http://www.cloudcompare.org/

Girod, L., Nielsen, N.I., Couderette, F., Nuth, C., Kääb, A., 2018. Precise DEM extraction from Svalbard using 1936 high oblique imagery. Geoscientific Instrumentation, Methods and Data Systems 7 (4), 277–288.

Gomez, C., 2014. Digital photogrammetry and GIS-based analysis of the bio-geomorphological evolution of Sakurajima Volcano, diachronic analysis from 1947 to 2006. J. Volcanol. Geotherm. Res. 280, 1–13.

Gomez, C., Hayakawa, Y., Obanawa, H., 2015. A study of Japanese landscapes using structure from motion derived DSMs and DEMs based on historical aerial photographs: new opportunities for vegetation monitoring and diachronic geomorphology. Geomorphology 242, 11–20.

Guerin, A., Abellán, A., Matasci, B., Jaboyedoff, M., Derron, M.H., Ravanel, L., 2017. Brief communication: 3-D reconstruction of a collapsed rock pillar from Web-retrieved images and terrestrial laser scanner data–the 2005 event of the west face of the Drus (Mont Blanc massif). Nat. Hazards Earth Syst. Sci. 17 (7), 1207–1220.

Guzzetti, F., Malamud, B.D., Turcotte, D.L., Reichenbach, P., 2002. Power-law correlations of landslide areas in central Italy. Earth Planet. Sci. Lett. 195 (3–4), 169–183.

Guzzetti, F., Reichenbach, P., Wieczorek, G.F., 2003. Rockfall hazard and risk assessment in the Yosemite Valley, California, USA. Nat. Hazards Earth Syst. Sci. 3 (6), 491–503.

Guzzetti, F., Ardizzone, F., Cardinali, M., Rossi, M., Valigi, D., 2009. Landslide volumes and landslide mobilization rates in Umbria, central Italy. Earth Planet. Sci. Lett. 279 (3–4), 222–229.

Hantz, D., 2011. Quantitative assessment of diffuse rock fall hazard along a cliff foot. Nat. Hazards Earth Syst. Sci. 11 (5), 1303–1309.

Hantz, D., Vengeon, J.M., Dussauge-Peisser, C., 2003. An historical, geomechanical and probabilistic approach to rock-fall hazard assessment. Nat. Hazards Earth Syst. Sci. 3 (6), 693–701.

Heckmann, T., Bimböse, M., Krautblatter, M., Haas, F., Becht, M., Morche, D., 2012. From geotechnical analysis to quantification and modelling using LiDAR data: a study on rockfall in the Reintal catchment, Bavarian Alps, Germany. Earth Surf. Process. Landf. 37 (1), 119–133.

Hexagon-Technodigit (2015): 3DReshaper: the 3-D Scanner Software (version 10.1.4). Technodigit part of Hexagon. Available from: https://www.3dreshaper.com/en/

Huber, N.K. (1987): The Geologic Story of Yosemite National Park. U.S. Geological Survey Bulletin 1595, 64 p.

Hungr, O., Evans, S.G., Hazzard, J., 1999. Magnitude and frequency of rock falls and rock slides along the main transportation corridors of southwestern British Columbia. Can. Geotech. J. 36 (2), 224–238.

Hungr, O., McDougall, S., Wise, M., Cullen, M., 2008. Magnitude–frequency relationships of debris flows and debris avalanches in relation to slope relief. Geomorphology 96 (3–4), 355–365.

Ishiguro, S., Yamano, H., Oguma, H., 2016. Evaluation of DSMs generated from multi-temporal aerial photographs using emerging structure from motion–multi-view stereo technology. Geomorphology 268, 64–71.

James, M.R., Robson, S., 2014. Mitigating systematic error in topographic models derived from UAV and ground-based image networks. Earth Surf. Process. Landf. 39 (10), 1413–1420.

Javernick, L., Brasington, J., Caruso, B., 2014. Modeling the topography of shallow braided rivers using Structure-from-Motion photogrammetry. Geomorphology 213, 166–182.

Kazhdan, M., Bolitho, M., Hoppe, H., 2006. Poisson surface reconstruction. In: Polthier, K., Sheffer, A. (Eds.), The Eurographics Association, Proceedings of the 4th Eurographics Symposium on Geometry Processing, pp. 61–70.

Kemeny, J., 2005. Time-dependent drift degradation due to the progressive failure of rock bridges along discontinuities. Int. J. Rock Mech. Min. Sci. 42 (1), 35–46.

Kiryati, N., Székely, G., 1993. Estimating shortest paths and minimal distances on digitized three-dimensional surfaces. Pattern Recogn. 26 (11), 1623–1637.

Krautblatter, M., Dikau, R., 2007. Towards a uniform concept for the comparison and extrapolation of rockwall retreat and rockfall supply. Geogr. Ann. 89A (1), 21–40.

Kromer, R.A., Hutchinson, D.J., Lato, M.J., Gauthier, D., Edwards, T., 2015. Identifying rock slope failure precursors using Lidar for transportation corridor hazard management. Eng. Geol. 195, 93–103.

Kumar, N.S., Ismail, M.A.M., Sukor, N.S.A., Cheang, W., 2018. Geohazard reconnaissance mapping for potential rock boulder fall using low altitude UAV photogrammetry. In: IOP Conference Series: Materials Science and Engineering 352, 012033 (7 p).

Lague, D., Brodu, N., Leroux, J., 2013. Accurate 3D comparison of complex topography with terrestrial laser scanner: application to the Rangitikei canyon (NZ). ISPRS J. Photogramm. Remote Sens. 82, 10–26.

Lari, S., Frattini, P., Crosta, G.B., 2014. A probabilistic approach for landslide hazard analysis. Eng. Geol. 182, 3–14.

Lato, M., Diederichs, M.S., Hutchinson, D.J., Harrap, R., 2009. Optimization of Lidar scanning and processing for automated structural evaluation of discontinuities in rockmasses. Int. J. Rock Mech. Min. Sci. 1 (46), 194–199.

Letortu, P., Costa, S., Cador, J.M., Coinaud, C., Cantat, O., 2015. Statistical and empirical analyses of the triggers of coastal chalk cliff failure. Earth Surf. Process. Landf. 40 (10), 1371–1386.

Lucieer, A., Jong, S.M.D., Turner, D., 2014. Mapping landslide displacements using Structure from Motion (SfM) and image correlation of multi-temporal UAV photography. Prog. Phys. Geogr. 38 (1), 97–116.

Luckman, B.H., 1976. Rockfalls and rockfall inventory data: some observations from Surprise Valley, Jasper National Park, Canada. Earth Surface Processes 1 (3), 287–298.

Malamud, B.D., Turcotte, D.L., Guzzetti, F., Reichenbach, P., 2004. Landslide inventories and their statistical properties. Earth Surf. Process. Landf. 29 (6), 687–711.

Manousakis, J., Zekkos, D., Saroglou, F., Clark, M., 2016. Comparison of UAV-enabled photogrammetry-based 3D point clouds and interpolated DSMs of sloping terrain for rockfall hazard analysis. The International Archives of Photogrammetry, Remote Sensing and Spatial Information Sciences 42, 71–77.

Martel, S.J., 2006. Effect of topographic curvature on near-surface stresses and application to sheeting joints. Geophys. Res. Lett. 33 (1), L01308 (5p).

Martel, S.J., 2011. Mechanics of curved surfaces, with application to surface-parallel cracks. Geophys. Res. Lett. 38 (20), L20303 (6p).

Matasci, B., Carrea, D., Jaboyedoff, M., Pedrazzini, A., Stock, G.M., Oppikofer, T., 2011. Structural characterization of rockfall sources in Yosemite Valley from remote sensing data: toward more accurate susceptibility assessment. In: Proceedings of the 64th Canadian Geotechnical Conference and the 14th Pan-American Conference on Soil Mechanics and Geotechnical Engineering (Vol. 54). Canadian Geotechnical Society.

Matasci, B., Stock, G.M., Jaboyedoff, M., Carrea, D., Collins, B.D., Guerin, A., Matasci, G., Ravanel, L., 2018. Assessing rockfall susceptibility in steep and overhanging slopes using three-dimensional analysis of failure mechanisms. Landslides 15 (5), 859–878.

Matsuoka, N., Sakai, H., 1999. Rockfall activity from an alpine cliff during thawing periods. Geomorphology 28, 309–328.

Matthes, F.E., 1930. Geologic history of the Yosemite Valley. U.S. Geol. Surv. Prof. Pap. 160, 137.

Mertes, J.R., Gulley, J.D., Benn, D.I., Thompson, S.S., Nicholson, L.I., 2017. Using structure-from-motion to create glacier DEMs and orthoimagery from historical terrestrial and oblique aerial imagery. Earth Surf. Process. Landf. 42 (14), 2350–2364.

Midgley, N.G., Tonkin, T.N., 2017. Reconstruction of former glacier surface topography from archive oblique aerial images. Geomorphology 282, 18–26.

Mölg, N., Bolch, T., 2017. Structure-from-motion using historical aerial images to analyse changes in glacier surface elevation. Remote Sens. 9 (10), 1021 (17 p).

Moore, J.R., Sanders, J.W., Dietrich, W.E., Glaser, S.D., 2009. Influence of rockmass strength on the erosion rate of alpine cliffs. Earth Surf. Process. Landf. 34, 1339–1352.

Oppikofer, T., Jaboyedoff, M., Blikra, L., Derron, M.H., Metzger, R., 2009. Characterization and monitoring of the Åknes rockslide using terrestrial laser scanning. Nat. Hazards Earth Syst. Sci. 9 (3), 1003–1019.

Teledyne Optech (2019): ILRIS-LR Terrestrial Laser Scanner, Summary Specifications Sheet. Available from: http://pdf.directindustry.com/pdf/optech/ilris-lr/25132-387459.html

Peck, D.L., 2002. Geologic map of the Yosemite quadrangle, central Sierra Nevada, California. U.S. Geological Survey Geologic Investigations Series Map GQ-1531.

Pedrazzini, A., Oppikofer, T., Jaboyedoff, M., Chantry, R., & Stampfli, E. (2010, June): Assessment of rockslide and rockfall problems in an active quarry: case study of the Arvel quarry (western Switzerland). In ISRM International Symposium-EUROCK 2010. International Society for Rock Mechanics and Rock Engineering.

Pellicani, R., Spilotro, G., Van Westen, C.J., 2016. Rockfall trajectory modeling combined with heuristic analysis for assessing the rockfall hazard along the Maratea SS18 coastal road (Basilicata, Southern Italy). Landslides 13 (5), 985–1003.

Petley, D.N., Higuchi, T., Petley, D.J., Bulmer, M.H., Cary, J., 2005. Development of progressive landslide failure in cohesive materials. Geology 33, 201–204.

Picarelli, L., Oboni, F., Evans, S.G., Mostyn, G., Fell, R., 2005. Hazard characterization and quantification. Landslide risk management 27–62.

Pickering, G., Bull, J.M., Sanderson, D.J., 1995. Sampling power-law distributions. Tectonophysics 248 (1–2), 1–20.

Pratt, C., Macciotta, R., & Hendry, M. (2018): Quantitative relationship between weather seasonality and rock fall occurrences north of Hope, BC, Canada. Bulletin of Engineering Geology and the Environment, 1–13.

Putnam, R., Glazner, A.F., Coleman, D.S., Kylander-Clark, A.R., Pavelsky, T., Abbot, M.I., 2015. Plutonism in three dimensions: Field and geochemical relations on the southeast face of El Capitan, Yosemite National Park, California. Geosphere 11 (4), 1133–1157.

Ravanel, L., Deline, P., 2008. La face ouest des Drus (massif du Mont-Blanc): évolution de l'instabilité d'une paroi rocheuse dans la haute montagne alpine depuis la fin du petit âge glaciaire. Géomorphologie: relief, processus, environnement 14 (4), 261–272.

Riquelme, A., Del Soldato, M., Tomás, R., Cano, M., Bordehore, L.J., & Moretti, S. (2019): Digital landform reconstruction using old and recent open access digital aerial photos. Geomorphology, 329, 206–223.

Roberti, G., Ward, B., de Vries, B.V.W., Friele, P., Perotti, L., Clague, J.J., Giardino, M., 2018. Precursory slope distress prior to the 2010 Mount Meager landslide. British Columbia. Landslides 15 (4), 637–647.

Rood, D.H., Burbank, D.W., Finkel, R.C., 2011. Chronology of glaciations in the Sierra Nevada, California, from 10Be surface exposure dating. Quat. Sci. Rev. 30 (5–6), 646–661.

Rosnell, T., Honkavaara, E., 2012. Point cloud generation from aerial image data acquired by a quadrocopter type micro unmanned aerial vehicle and a digital still camera. Sensors 12 (1), 453–480.

Rosser, N.J., Petley, D.N., Lim, M., Dunning, S.A., Allison, R.J., 2005. Terrestrial laser scanning for monitoring the process of hard rock coastal cliff erosion. Q. J. Eng. Geol. Hydrogeol. 38 (4), 363–375.

Rossi, M., Witt, A., Guzzetti, F., Malamud, B.D., Peruccacci, S., 2010. Analysis of historical landslide time series in the Emilia-Romagna region, northern Italy. Earth Surf. Process. Landf. 35 (10), 1123–1137.

Rowe, E., Hutchinson, D.J., Kromer, R.A., 2018. An analysis of failure mechanism constraints on pre-failure rock block deformation using TLS and roto-translation methods. Landslides 15 (3), 409–421.

Royán, M.J., Abellán, A., Jaboyedoff, M., Vilaplana, J.M., Calvet, J., 2014. Spatio-temporal analysis of rockfall pre-failure deformation using Terrestrial Lidar. Landslides 11 (4), 697–709.

Ruggles, S., Clark, J., Franke, K.W., Wolfe, D., Reimschiissel, B., Martin, R.A., Okeson, T., Hedengren, J.D., 2016. Comparison of SfM computer vision point clouds of a landslide derived from multiple small UAV platforms and sensors to a TLS-based model. Journal of Unmanned Vehicle Systems 4 (4), 246–265.

Sass, O., Oberlechner, M., 2012. Is climate change causing increased rockfall frequency in Austria? Nat. Hazards Earth Syst. Sci. 12 (11), 3209–3216.

Smith, M.W., Carrivick, J.L., Quincey, D.J., 2016. Structure from motion photogrammetry in physical geography. Prog. Phys. Geogr. 40 (2), 247–275.

Snyder, J.B. (1986): Anatomy of a rockslide. Yosemite, 48(3), 4–5 & 12.

Snyder, J.B., 1996. The ground shook and the sky fell. Yosemite 58 (4), 2–9.

Stark, C.P., Hovius, N., 2001. The characterization of landslide size distributions. Geophys. Res. Lett. 28 (6), 1091–1094.

Stock, G.M., Uhrhammer, R.A., 2010. Catastrophic rock avalanche 3600 years BP from El Capitan, Yosemite Valley, California. Earth Surf. Process. Landf. 35 (8), 941–951.

Stock, G.M., Anderson, R.S., Finkel, R.C., 2005. Rates of erosion and topographic evolution of the Sierra Nevada, California, inferred from cosmogenic ^{26}Al and ^{10}Be concentrations. Earth Surf. Process. Landf. 30, 985–1006.

Stock, G.M., Bawden, G.W., Green, J.K., Hanson, E., Downing, G., Collins, B.D., Bond, S., Leslar, M., 2011. High-resolution three-dimensional imaging and analysis of rock falls in Yosemite Valley, California. Geosphere 7 (2), 573–581.

Stock, G.M., Martel, S.J., Collins, B.D., Harp, E.L., 2012. Progressive failure of sheeted rock slopes: the 2009–2010 Rhombus Wall rock falls in Yosemite Valley, California, USA. Earth Surf. Process. Landf. 37 (5), 546–561.

Stock, G.M., Collins, B.D., Santaniello, D.J., Zimmer, V.L., Wieczorek, G.F., & Snyder, J.B. (2013): Historical Rock Falls in Yosemite National Park, California (1857-2011). U.S. Geological Survey Data Series 746, 17 p.

Stock, G.M., Guerin, A., Avdievitch, N., Collins, B.D., Jaboyedoff, M., 2018. Rapid 3-D analysis of rockfalls. GSA Today 28 (8), 28–29.

Strunden, J., Ehlers, T.A., Brehm, D., Nettesheim, M., 2015. Spatial and temporal variations in rockfall determined from TLS measurements in a deglaciated valley, Switzerland. J. Geophys. Res. Earth Surf. 120 (7), 1251–1273.

Tanyaş, H., Van Westen, C.J., Allstadt, K.E., Anna Nowicki Jessee, M., Görüm, T., Jibson, R.W., Godt, J.W., Sato, H.P., Schmitt, R.G., Marc, O., & Hovius, N. (2017): Presentation and analysis of a worldwide database of earthquake-induced landslide inventories. J. Geophys. Res. Earth Surf., 122(10), 1991–2015.

Teza, G., Galgaro, A., Zaltron, N., Genevois, R., 2007. Terrestrial laser scanner to detect landslide displacement fields: a new approach. Int. J. Remote Sens. 28 (16), 3425–3446.

Tonini, M., Abellán, A., 2014. Rockfall detection from terrestrial Lidar point clouds: A clustering approach using R. Journal of Spatial Information Science 2014 (8), 95–110.

Tonkin, T.N., Midgley, N.G., Cook, S.J., Graham, D.J., 2016. Ice-cored moraine degradation mapped and quantified using an unmanned aerial vehicle: a case study from a polythermal glacier in Svalbard. Geomorphology 258, 1–10.

Török, Á., Barsi, Á., Bögöly, G., Lovas, T., Somogyi, Á., Görög, P., 2018. Slope stability and rockfall assessment of volcanic tuffs using RPAS with 2-D FEM slope modelling. Nat. Hazards Earth Syst. Sci. 18 (2), 583–597.

Valagussa, A., Frattini, P., Crosta, G.B., 2014. Earthquake-induced rockfall hazard zoning. Eng. Geol. 182, 213–225.

Vautier, F., Corenblit, D., Hortobágyi, B., Fafournoux, L., Steiger, J., 2016. Monitoring and reconstructing past biogeomorphic succession within fluvial corridors using stereophotogrammetry. Earth Surf. Process. Landf. 41 (10), 1448–1463.

van Veen, M., Hutchinson, D.J., Kromer, R.A., Lato, M., Edwards, T., 2017. Effects of sampling interval on the frequency-magnitude relationship of rockfalls detected from terrestrial laser scanning using semi-automated methods. Landslides 14 (5), 1579–1592.

Voumard, J., Abellán, A., Nicolet, P., Penna, I., Chanut, M.A., Derron, M.H., Jaboyedoff, M., 2017. Using street view imagery for 3-D survey of rock slope failures. Nat. Hazards Earth Syst. Sci. 17 (12), 2093–2107.

Voumard, J., Derron, M.H., Jaboyedoff, M., 2018. Natural hazard events affecting transportation networks in Switzerland from 2012 to 2016. Nat. Hazards Earth Syst. Sci. 18 (8), 2093–2109.

Wahrhaftig, C., Stock, G.M., McCracken, R.G., Sasnett, P., Cyr, A.J., 2019. Extent of the Last Glacial Maximum. Tioga) glaciation in Yosemite National Park and vicinity, California. U.S. Geological Survey Scientific Investigations Map, p. 3414.

Warrick, J.A., Ritchie, A.C., Adelman, G., Adelman, K., Limber, P.W., 2016. New techniques to measure cliff change from historical oblique aerial photographs and structure-from-motion photogrammetry. J. Coast. Res. 33 (1), 39–55.

Westoby, M.J., Brasington, J., Glasser, N.F., Hambrey, M.J., & Reynolds, J.M. (2012): 'Structure-from-Motion'photogrammetry: a low-cost, effective tool for geoscience applications. Geomorphology, 179, 300–314.

Wieczorek, G.F. (2002): Catastrophic rockfalls and rockslides in the Sierra Nevada, USA. In: Evans, S.G., & DeGraff, J.V. (Eds.), Catastrophic Landslides: Effects, Occurrence, and Mechanisms. The Geological Society of America, Reviews in Engineering Geology, 15, 165–190.

Wieczorek, G.F., Jäger, S., 1996. Triggering mechanisms and depositional rates of postglacial slope-movement processes in the Yosemite Valley, California. Geomorphology 15 (1), 17–31.

Wieczorek, G.F., Snyder, J.B., 1999. Rock falls from Glacier Point above Camp Curry, Yosemite National Park, California. U.S. Geological Survey Open-File Report 99-385, 22.

Wieczorek, G.F., Snyder, J.B., 2004. Historical rock falls in Yosemite National Park, California. U.S. Geological Survey Open-File Report 3-491, 10.

Wieczorek, G.F., Snyder, J.B., Alger, C.S., & Issacson, K.A. (1992): Rock falls in Yosemite Valley, California. U.S. Geological Survey Open-File Report 92-387, 191 p.

Wieczorek, G.F., Nishenko, S.P., Varnes, D.J., 1995. Analysis of rock falls in the Yosemite Valley, California. In: Daemen, J.J.K., Schultz, R.A. (Eds.), Rock Mechanics: American Rock Mechanics Association, Proceedings of the 35th U.S. Symposium on Rock Mechanics, June 5–7, 1995, Reno, Nev, pp. 85–89.

Wieczorek, G.F., Morrissey, M.M., Iovine, G., Godt, J., 1999. Rock-fall potential in the Yosemite Valley, California. U.S. Geological Survey Open-File Report 99-578.

Wieczorek, G.F., Snyder, J.B., Waitt, R.B., Morrissey, M.M., Uhrhammer, R., Harp, E.L., Norris, R.D., Bursik, M.I., Finewood, L.G., 2000. The unusual air blast and dense sandy cloud triggered by the July 10, 1996, rock fall at Happy Isles, Yosemite National Park, California. Geol. Soc. Am. Bull. 112 (1), 75–85.

Wieczorek, G.F., Stock, G.M., Reichenbach, P., Snyder, J.B., Borchers, J.W., Godt, J.W., 2008. Investigation and hazard assessment of the 2003 and 2007 Staircase Falls rock falls, Yosemite National Park, California, USA. Nat. Hazards Earth Syst. Sci. 8 (3), 421–432.

Williams, J.G., Rosser, N.J., Hardy, R.J., Brain, M.J., Afana, A.A., 2018. Optimising 4-D surface change detection: an approach for capturing rockfall magnitude–frequency. Earth Surface Dynamics 6 (1), 101–119.

Williams, J.G., Rosser, N.J., Hardy, R.J., Brain, M.J., 2019. The Importance of monitoring Interval for Rockfall Magnitude-Frequency Estimation. J. Geophys. Res. Earth Surf. 124, 1–13.

Woo, H., Kang, E., Wang, S., Lee, K.H., 2002. A new segmentation method for point cloud data. Int. J. Mach. Tools Manuf. 42 (2), 167–178.

Zhang, Y., Yue, P., Zhang, G., Guan, T., Lv, M., Zhong, D., 2019. Augmented reality mapping of rock mass discontinuities and rockfall susceptibility based on unmanned aerial vehicle photogrammetry. Remote Sens. 11 (11), 1311 (34 p).

Zhang, Z., 1994. Iterative point matching for registration of free-form curves and surfaces. Int. J. Comput. Vis. 13 (2), 119–152.

Zimmer, V.L., Collins, B.D., Stock, G.M., Sitar, N., 2012. Rock fall dynamics and deposition: an integrated analysis of the 2009 Ahwiyah Point rock fall, Yosemite National Park, USA. Earth Surf. Process. Landf. 37 (6), 680–691.